Chemical Geology 611 (2022) 121117

Contents lists available at ScienceDirect

Chemical Geology

journal homepage: www.elsevier.com/locate/chemgeo

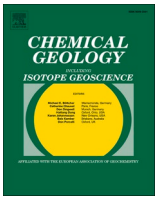

Mantle plume-subducted oceanic slab interaction contributes to geochemical heterogeneity of the Emeishan large igneous province

Zhong-Jie Bai [a,*], Hong Zhong [a,b], Wei-Guang Zhu [a], Wen-Jun Hu [a]

[a] State Key Laboratory of Ore Deposit Geochemistry, Institute of Geochemistry, Chinese Academy of Sciences, Guiyang 550081, China
[b] University of Chinese Academy of Sciences, Beijing 100049, China

ARTICLE INFO

Editor: Dr. S Aulbach

Keywords:
Emeishan large igneous province
Hongge mafic–ultramafic intrusion
Mantle source
Mantle plume–subducted slab interaction
Paleo-Tethyan oceanic crust

ABSTRACT

Mantle-derived rocks in large igneous provinces yield large variations in their chemical and isotopic compositions as well as redox conditions; however, the origin of these heterogeneities remains unclear. We present new geochemical and Sr–Nd–Hf–O isotopic data for the Hongge mafic–ultramafic intrusion and associated syenite in the Emeishan large igneous province (ELIP), and combine them with previously published data from coeval intrusive and volcanic rocks in the ELIP, to constrain the generation of the ELIP and associated world-class Fe–Ti–V oxide deposits. The rocks from the marginal zone of the Hongge intrusion have high-Ti basaltic-like compositions with high initial $^{87}Sr/^{86}Sr$ ratios (0.7084–0.7096) and unradiogenic ε_{Nd} (−7.7 to −5.9) and ε_{Hf} (−6.0 to −2.4) values, and represent the most enriched endmember of the high-Ti basaltic series observed in the ELIP to date. The marginal zone rocks, temporally and spatially associated basalts, and syenites yield depleted Zr and Hf contents with Zr/Sm (7.1–38.3) and Hf/Nd (0.05–0.12) ratios between those of marine sediment and OIB. The Nd—Hf isotopic compositions of the marginal zone rocks plot above the terrestrial array, suggesting decoupling between Nd and Hf isotopic compositions. Mixing between subducted oceanic crusts, marine sediments and mantle peridotite accounts for the enriched Sr—Nd isotopic compositions, Zr—Hf depletion, and the decoupling between Nd and Hf isotopic compositions in these samples as well as in other mafic–felsic intrusions of the ELIP. Zircon grains from the syenites yield more radiogenic ε_{Hf} values (+3.7 − +6.6) than the marginal zone rocks and have $\delta^{18}O$ values of 3.9–5.7‰, most of which are much lower than mantle-zircon values, suggesting that oceanic crust altered at high temperature was involved in the mantle source. The integrated Sr–Nd–Hf–O isotopic compositions of these mafic–felsic intrusions can be explained by a model for the generation of the ELIP whereby a mantle plume interacted with the subducted Paleo-Tethyan oceanic lithospheric slab and overlying marine sediment. Our results suggest that the inclusion of the recycled altered oceanic slab in the mantle source of the ELIP led to its geochemical and, potentially, redox heterogeneity.

1. Introduction

Large igneous provinces (LIPs) are formed by the rapid emplacement of large volumes of intraplate mafic–ultramafic magma and associated silicic magmas in the crust, and thus have geological and environmental impacts that are regional to global in scale (Bryan and Ernst, 2008). Although various mechanisms have been proposed for the origin of LIPs, the basalts found in LIPs often yield OIB-like geochemical compositions and are generally thought to result from decompression melting of a mantle plume rising from the core–mantle boundary (Campbell and Griffiths, 1990). Magmas from LIPs are geochemically and isotopically heterogeneous. In particular, enriched crustal signatures have been identified in these OIB-like mantle-derived magmas, whose origin, however, is not well understood. It has been proposed that the enriched geochemical compositions were inherited from ancient recycled oceanic slab and sediment that had been subducted to the core–mantle boundary and then returned to the surface by a mantle plume (Eiler et al., 1997; Hofmann and White, 1982; Jackson et al., 2007). In addition to the geochemical heterogeneity, redox heterogeneity has also been identified in some LIPs and hotspots (Bai et al., 2019; Moussallam et al., 2019; Wu et al., 2022). Mid-ocean ridge basalts (MORBs), which are formed by the partial melting of the upper mantle uninfluenced by mantle plumes, also display large variations in geochemical and isotopic compositions. The compositional heterogeneity of MORB has been linked to the recycling

* Corresponding author.
E-mail address: baizhongjie@vip.gyig.ac.cn (Z.-J. Bai).

https://doi.org/10.1016/j.chemgeo.2022.121117
Received 22 July 2022; Received in revised form 12 September 2022; Accepted 13 September 2022
Available online 16 September 2022

of oceanic slabs in the upper mantle (Eiler et al., 2000; Rehkämper and Hofmann, 1997). A mantle plume rising from depth to the base of the lithospheric mantle might, therefore, interact with recycled oceanic slabs already existing in the upper mantle; however, it is still unclear whether this contributes to the geochemical and redox heterogeneity in LIPs. LIPs are also economically important due to their direct and indirect links to various types of orthomagmatic and hydrothermal mineral deposits (Ernst and Jowitt, 2013). The type and size of ore deposits associated with each LIP are highly variable. Only a few LIPs are known to be associated with giant Fe–Ti–V oxide deposits, and the factors controlling the metallogenic potential of Fe–Ti–V oxide deposits in LIPs are still unclear.

Similar to lavas from other LIPs, the OIB-like mantle-derived lavas of the Permian Emeishan LIP (ELIP) show large variations in geochemical and isotopic compositions. Ancient recycled oceanic crust and its secondary product (pyroxenite) have been suggested to contribute to the geochemical heterogeneity of the magmatism in the ELIP (Hou et al., 2011; Ren et al., 2017; Yu et al., 2017; Liu et al., 2022). Mafic–ultramafic intrusions form part of the ELIP and host the largest Fe–Ti–V oxide deposits in the world. In this paper, we combine new whole-rock chemical and Sr-Nd-Hf isotopic data as well as zircon Hf—O isotopic data from the Hongge mafic–ultramafic intrusion and temporally and spatially associated syenite in the ELIP with previously published data from coeval intrusive and volcanic rocks from the ELIP, which provide the first robust evidence for the presence of subducted marine sediments in the source of the magmas. Our results demonstrate that the interaction between subducted oceanic slabs and mantle plumes plays an important role in producing chemical and redox heterogeneity in LIPs as well as the formation of world-class Fe–Ti–V oxide deposits.

2. Geologic setting and sample descriptions

The ELIP is located to the east of the East Paleo-Tethys suture zone and on the western margin of the Yangtze Block, SW China (Fig. 1a). The basement of the Yangtze Block consists of the Paleoproterozoic–Mesoproterozoic low-grade metasedimentary and metavolcanic rocks of the Huili and Kunyang groups and the Neoproterozoic amphibolite to granulite facies metamorphic rocks of the Kangding Complex. The basement is overlain by a thick cover of Neoproterozoic metasedimentary rocks and Paleozoic carbonates. It is thought that the ELIP is genetically associated with the Emeishan mantle plume (Chung and Jahn, 1995). The ELIP crops out over an area of 5×10^5 km^2 and consists of continental flood basalts, mafic–ultramafic intrusions, and associated felsic syenite and granite that were erupted or emplaced at ~260 Ma. The main Paleo-Tethys Ocean slab was subducted to the east beneath the Yangtze Block during this time and closed along the Changning–Menglian suture zone at ~240 Ma (Wang et al., 2018).

The volcanic sequence varies in thickness from 5 km in the west to

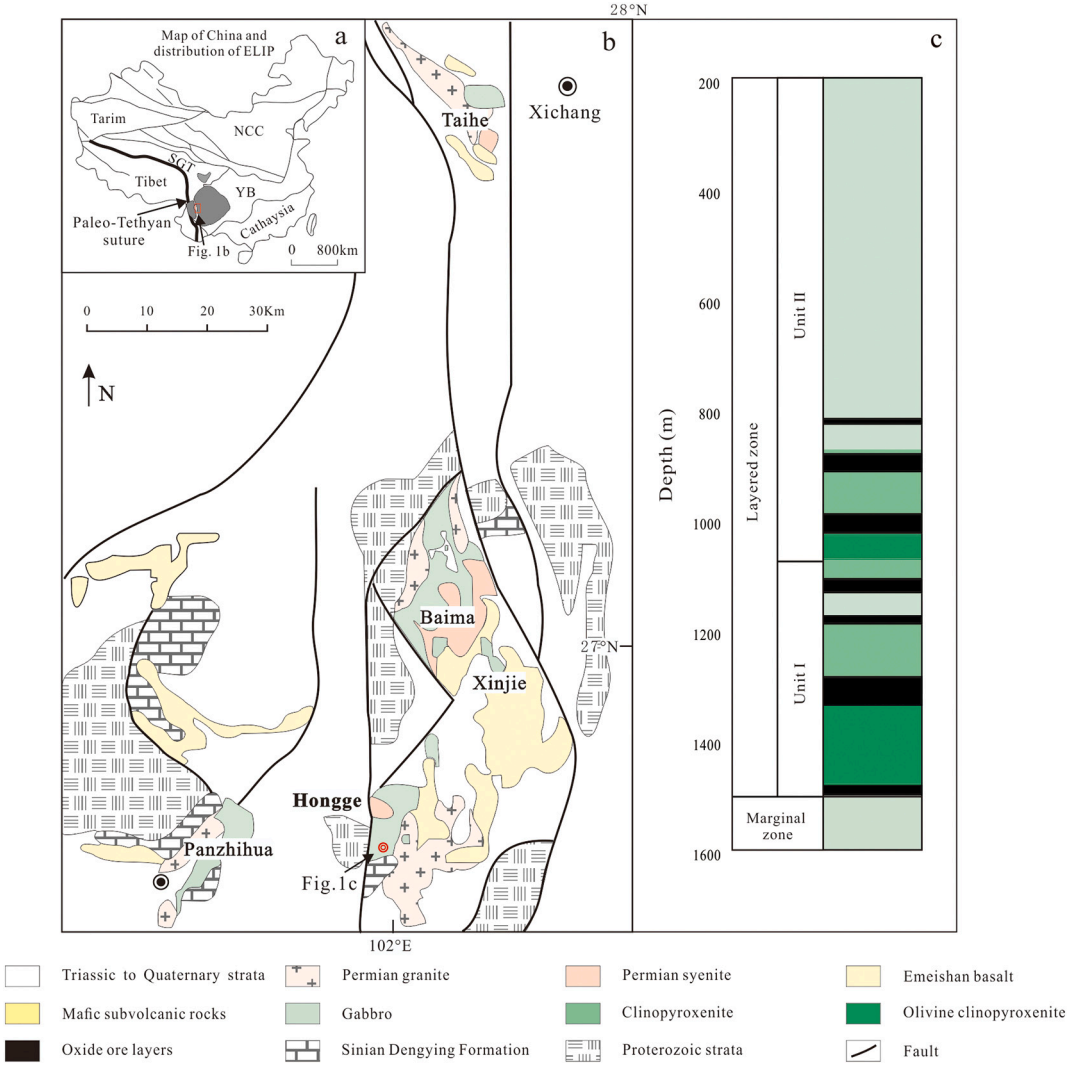

Fig. 1. Geologic maps of (a) the Emeishan large igneous province and the Paleo-Tethyan suture, and (b) Fe—Ti oxide-mineralized intrusions in the Pan–Xi region. (c) Composite stratigraphic column for the Hongge mafic–ultramafic intrusion.

several hundred meters in the east of the ELIP. It consists of basalts with minor picrites, basaltic andesites, and rhyolitic or trachytic flows. The Emeishan basalts are subdivided into high-Ti (Ti/Y > 500) and low-Ti (Ti/Y < 500) series (Xu et al., 2001). In the inner zone of the ELIP, known as the Panzhihua–Xichang (Pan–Xi) region, the volcanic sequence has been eroded away as a result of deformation and uplift. Remnant volcanic rocks are generally exposed in the middle and outer zones of the ELIP (Fig. 1b); therefore, the intrusive rocks of the ELIP, dominated by mafic–ultramafic intrusions, granites, and syenites, are generally exposed in the inner zone (Fig. 1b). Some of the mafic–ultramafic intrusions (including the Hongge, Panzhihua, Baima, and Taihe intrusions) host world-class Fe–Ti–V oxide deposits, constituting the largest Fe–Ti–V ore district in the world. Previous studies have suggested that the compositions of the parental magmas of these intrusions are similar to those of the coeval Emeishan high-Ti basalts, which evolved from high-Ti picritic magma by extensive fractional crystallization (Bai et al., 2012, 2019; Zhou et al., 2008; Pang et al., 2010). Most of the syenites and A-type granites are temporally and spatially associated with the Fe–Ti–V oxide mineralized mafic–ultramafic intrusions (Fig. 1b). It has been suggested that the mafic–ultramafic and spatially associated felsic intrusions represent the cumulates and residual melts, respectively, of a basaltic magma (Zhong et al., 2007; Shellnutt et al., 2009b). Sporadically distributed Emeishan basalts crop out close to the mafic–ultramafic intrusions within the Pan–Xi region (Fig. 1b).

The sill-like Hongge mafic–ultramafic layered intrusion is 16 km long, 1.5 km thick, and hosts the largest magmatic Fe–Ti–V oxide deposit in the ELIP, comprising 4572 Mt. of oxide ores with 1.83×10^9 t of Fe, 1.96×10^8 t of Ti, and 1.45×10^7 t of V (Ma et al., 2003). The intrusion was emplaced into the Proterozoic metamorphosed volcano-sedimentary rocks and dolomitic limestones of the Sinian Dengying Formation at 259.3 ± 1.3 Ma (Zhong and Zhu, 2006). Contemporaneous alkaline syenites and I-type granites cover the intrusion and are overlain by the Emeishan flood basalts. This intrusion has been divided into a marginal zone consisting of fine-grained rocks at the base and an overlying layered zone consisting mainly of coarse-grained cumulates (Bai et al., 2021). Based on cumulus mineral stratigraphy, the layered series is further divided into two megacyclic units defined by a systematic upward progression from a basal olivine-clinopyroxenite, through Fe—Ti oxide-rich clinopyroxenite and disseminated and massive Fe—Ti oxide ore layers, to apatite-rich gabbro at the top (Fig. 1c). The Sr–Nd–Hf isotopic compositions of the syenites (Wang et al., 2013, 2015) are similar to those of the layered series of the Hongge intrusion, suggesting that they were derived from a common parental magma. In contrast, it has been suggested that the I-type granites were derived from partial melting of the middle–upper crustal Paleoproterozoic–Mesoproterozoic metasedimentary and metavolcanic rocks of the Huili group and juvenile underplated mantle-derived mafic rocks (Zhong et al., 2007).

We studied a 120 m-long drill core from the marginal zone in the southern part of the Hongge intrusion. This basal marginal zone consists of fine-grained gabbro in contact with metamorphosed sandstone host rocks (Fig. 2a) and olivine-phyric gabbro that lies between the fine-grained gabbro and the coarse-grained layered cumulates. The fine-grained gabbro is generally equigranular with grain sizes of ~50–100 μm and consists of clinopyroxene, plagioclase, and Fe–Ti–V oxides with accessory hornblende and biotite (Fig. 2b). The olivine–phyric gabbro contains large (~500 μm) olivine grains in a finer-grained matrix, similar to the underlying fine-grained gabbro (Fig. 2c). The syenite plutons covering the layered zone are composed of K-feldspar, albite, and arfvedsonite along with minor plagioclase and biotite (Fig. 2d). Six samples of olivine-phyric gabbro and 12 samples of fine-grained gabbro from the marginal zone of the Hongge intrusion were collected from the drill core at 5- to 10-m intervals. Three syenites were collected from the surface in the northern part of the Hongge intrusion. Zircon grains were separated from the syenites using conventional heavy liquid separation techniques and then hand-picked under a binocular microscope.

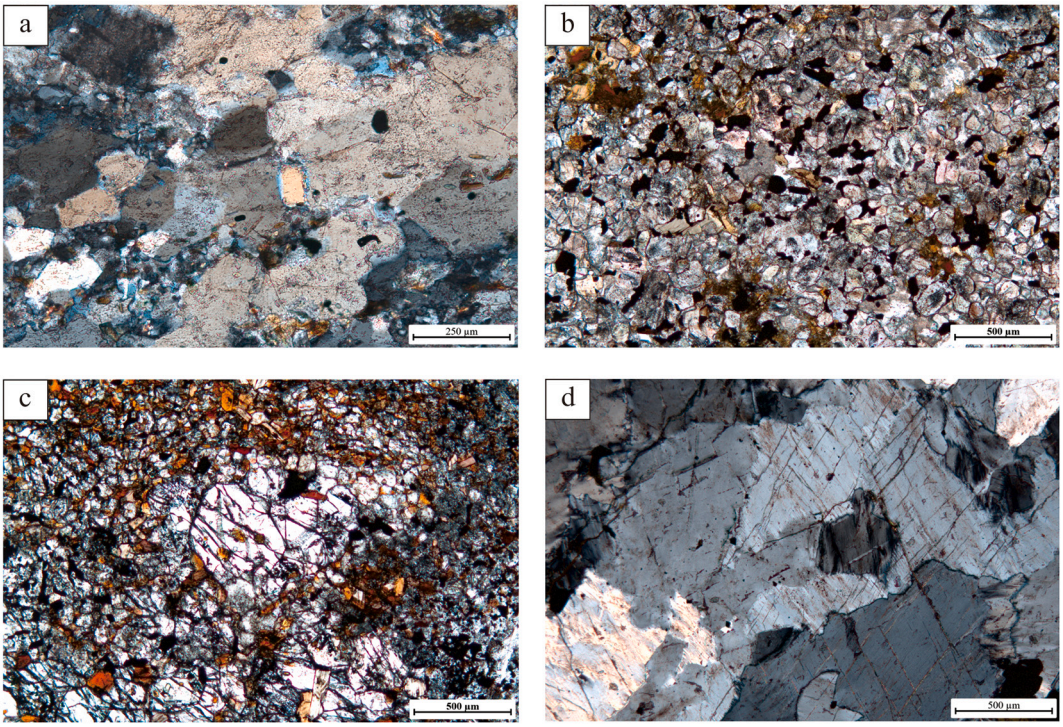

Fig. 2. Photomicrographs showing representative rock textures in the Hongge intrusion and associated syenite. (a) Metamorphosed sandstone wall rock. (b) Equigranular fine-grained gabbro from the marginal zone. (c) Olivine-phyric gabbro from the marginal zone with large olivine grains in a fine-grained matrix. (d) Coarse-grained syenite.

3. Analytical methods

Whole-rock major element compositions were determined using X-ray fluorescence spectrometry at the ALS Laboratory Group, Guangzhou, China, with an analytical precision of <5%. Whole-rock trace element compositions were determined using a PerkinElmer SCIEX ELAN DRC-e quadrupole inductively coupled plasma–mass spectrometer (ICP–MS) housed at the State Key Laboratory of Ore Deposit Geochemistry (SKLODG), Institute of Geochemistry, Chinese Academy of Sciences (CAS), Guiyang, China. Prior to analysis, powdered samples (50 mg) were dissolved in a HF + HNO_3 mixture in high-pressure Teflon bombs for 48 h at ~190 °C. Rhodium was used as an internal standard to correct matrix effects and instrument drift (Qi et al., 2000). The reference material BCR-2 was analyzed as unknowns to monitor analytical accuracy, and the result agrees well with the accepted values (Table 1).

Whole-rock Rb—Sr and Sm—Nd isotopic compositions were determined using a Nu Plasma II multicollector (MC)–ICP–MS at the State Key Laboratory of Environmental Geochemistry, Institute of Geochemistry, CAS. Before analysis, ~100 mg aliquots of sample powder were dissolved in closed Teflon beakers using a mixed HF–HNO_3–$HClO_4$ acid solution. Sr and Nd were extracted using AG 50 W-X12 cation-exchange resin and P507 extraction chromatography resin, respectively (Yang et al., 2010). Mass fractionation corrections for Sr and Nd isotopic ratios assumed an $^{86}Sr/^{88}Sr$ ratio of 0.1194 and a $^{146}Nd/^{144}Nd$ ratio of 0.7219, respectively. Repeat analysis of the NBS-987 Sr standard and the JNdi-1 Nd standard yielded a mean $^{87}Sr/^{86}Sr$ ratio of 0.710261 ± 0.00005 (2σ, $n = 10$) and a mean $^{143}Nd/^{144}Nd$ ratio of 0.512066 ± 0.000005 (2σ, $n = 8$), respectively. Analysis of the BCR-2 standard yielded $^{87}Sr/^{86}Sr$ and $^{143}Nd/^{144}Nd$ ratios of 0.704990 ± 0.000006 (2σ) and 0.512601 ± 0.000005 (2σ), respectively. The results of these standard reference materials agree well with the certified values (Table 2). Initial isotopic ratios were determined using Rb, Sr, Sm, and Nd contents measured by ICP–MS.

Whole-rock Lu—Hf isotopic compositions were determined using a Thermo Fisher Scientific Neptune Plus MC–ICP–MS at Beijing Createch Testing Technology, Beijing, China. Approximately 150 mg of each powdered sample was digested in high-pressure PTFE bombs with 2 ml of concentrated HNO_3 and 3 ml of concentrated HF. Hf was purified using LN resin (TrisKem, 100–150 μm) (Yang et al., 2010). A $^{176}Lu/^{175}Lu$ ratio of 0.02658 and a $^{176}Yb/^{173}Yb$ ratio of 0.796218 were used to correct for instrumental mass bias on Yb, Lu, and Hf isotopes and isobaric interferences of ^{176}Lu and ^{176}Yb, respectively, on ^{176}Hf contents. Detailed analytical procedures and correction methods are the same as those in Chu et al. (2009) and Yang et al. (2010). To correct for instrumental mass bias, Yb isotope ratios were normalized to a $^{172}Yb/^{173}Yb$ ratio of 1.35274 and Hf isotope ratios to a $^{179}Hf/^{177}Hf$ ratio of 0.7325 using an exponential function. The mass bias behavior of Lu was assumed to follow that of Yb. In addition, the stability of the $^{176}Hf/^{177}Hf$ ratio was assessed using the in-house GSB-Hf standard, which yielded a mean $^{176}Hf/^{177}Hf$ ratio of 0.282208 ± 0.000009 (2SD, $n = 9$). The measured $^{176}Hf/^{177}Hf$ ratios of the basaltic BHVO-2 and BCR-2 standards were 0.283115 and 0.282864, respectively. The results of these standard reference materials agree well with the accepted values (Table 2).

Zircon oxygen isotopic compositions were measured using a CAMECA 1280 secondary ion mass spectrometer (SIMS) at the Institute of Geology and Geophysics, CAS. Detailed working conditions and analytical procedures are described by Li et al. (2010). The Cs^+ primary ion beam was accelerated at 10 kV with an intensity of ~2 nA. The beam size was about 10 × 20 μm. Oxygen isotopes were measured in multi-collector mode using two off-axis Faraday cups. The internal precision of a single $^{18}O/^{16}O$ analysis was generally better than <0.2‰. $\delta^{18}O$ values were first normalized to V-SMOW (Vienna Standard Mean Ocean Water) values and are reported in standard per mil notation. Instrumental mass fractionation was corrected using zircon 91,500 as a reference. Analysis of the Penglai and Qinghu zircon standards yielded $\delta^{18}O$ of 5.27 ± 0.30 (7) and 5.41 ± 0.28 (3), respectively. The results of these standard reference materials agree well with the accepted values (Table 2).

In situ zircon Hf isotopic analyses were carried out using a Nu Plasma III MC–ICP–MS equipped with a RESOlution-LR laser ablation system at the SKLODG, with operating conditions and data acquisition methods similar to those described by Hu et al. (2012). The 193 nm ArF excimer laser, homogenized by a set of beam delivery systems, was focused on the zircon surface with a fluence of 6.0 J/cm^2 using a beam diameter of 40 μm and a repetition rate of 6 Hz for 40 s (equating to 240 pulses). The effect of instrumental mass bias on Hf isotopic compositions was corrected using an exponential function and assuming a $^{179}Hf/^{177}Hf$ ratio of 0.7325. Isobaric interference of ^{176}Lu and ^{176}Yb on ^{176}Hf contents was corrected using a $^{176}Yb/^{173}Yb$ ratio of 0.7962 and a $^{176}Lu/^{175}Lu$ ratio of 0.02655, respectively, with an exponential mass bias correction that assumed a $^{173}Yb/^{171}Yb$ ratio of 1.129197. Five standard zircons (GJ-1, 91,500, Plešovice, Mud Tank, Penglai) were analyzed after every 30 unknown samples, and 1 standard zircon (Penglai) was analyzed after every 5 unknown samples as quality control. The results of these standard reference materials are listed in Table 3, which agree well with the accepted values.

4. Results

4.1. Major and trace elements

The major and trace element compositions of the samples are listed in Table 1. Loss on ignition (LOI) values of the samples are 0.3–4.2 wt%, and most of the values are <2 wt%, which is consistent with the fact that the samples have only suffered very slight alteration (Fig. 2). Such a weakened degree of alteration would not have a significant impact on the geochemical compositions, especially for the alteration-resistant incompatible trace elements such as high field strength elements and REEs (Jenner, 1996).

At the base of the marginal zone, the fine-grained gabbro generally yields basaltic major and trace element compositions with relatively high TiO_2 contents. The fine-grained gabbro samples yield slightly higher MgO, CaO, Fe_2O_{3T}, Cr, and Ni contents and lower SiO_2 contents than the temporally and spatially associated Emeishan High-Ti basalts that overlie the Hongge intrusion (Fig. 3; Liao et al., 2015). The olivine-phyric gabbro samples have homogeneous compositions with high MgO (23.0–23.9 wt%), Cr (1240–1540 ppm), and Ni (933–1060 ppm) contents, which is consistent with the effect of olivine plus minor Cr-rich Fe—Ti oxides accumulation in these samples. The relatively low contents of incompatible trace elements in these samples are consistent with dilution by olivine accumulation. The syenites have the highest SiO_2 and the lowest CaO, Fe_2O_{3T}, TiO_2, Cr, and Ni contents in these igneous rocks.

The marginal gabbros and the syenites yield similar chondrite-normalized rare earth element (REE) patterns and primitive-mantle-normalized trace element patterns to those of the coeval high-Ti basalts (Fig. 4). Except for the syenites, no sample yields an Eu anomaly, in contrast to the coarse-grained gabbro from the ELIP intrusions (e.g. Pang et al., 2010). All the samples are characterized by strong depletion in Zr and Hf relative to neighboring elements on a spider diagram (Fig. 4). The Zr/Sm and Hf/Nd ratios of these rocks (Fig. 5) are lower than those of primitive mantle (McDonough and Sun, 1995), OIB (Sun and McDonough, 1989), and Yangtze upper crust (Gao et al., 1998). In contrast, the footwall sedimentary rocks are characterized by positive Zr—Hf anomalies on a trace element spider diagram (Fig. 4).

4.2. Whole-rock Sr–Nd–Hf isotopic compositions of the marginal zone

The Sr–Nd–Hf isotopic compositions of the samples from the marginal zone of the Hongge intrusion are listed in Table 2. These samples have highly radiogenic initial $^{87}Sr/^{86}Sr$ ratios (0.7084–0.7096) and unradiogenic $^{143}Nd/^{144}Nd$ ratios ($\varepsilon_{Nd(t)}$ = −5.85 to −7.70). These

Table 1
Major (wt%) and trace element (ppm) composition of the marginal zone of the Hongge mafic-ultramafic intrusion and associated syenite.

Sample	HG01	HG04	HG05	HG06	HG07	HG09	HG10	HG11	HG12	HG13	HG14	HG15
Rock type	wall-rock	gabbro	gabbro	gabbro	gabbro	gabbro	gabbro	gabbro	gabbro	gabbro	gabbro	gabbro
SiO_2	82.87	41.27	43.58	43.63	42.11	42.04	42.50	44.63	45.45	45.39	45.96	46.85
TiO_2	0.51	4.15	3.86	4.12	3.57	3.47	3.83	3.88	3.75	3.70	3.61	3.60
Al_2O_3	7.90	5.08	6.24	5.61	6.01	6.75	6.73	6.91	7.94	7.77	8.15	8.34
$Fe_2O_3^T$	1.41	17.12	15.95	16.28	15.44	14.82	15.78	15.40	14.76	14.89	14.69	13.96
MnO	0.02	0.23	0.30	0.24	0.19	0.20	0.26	0.22	0.18	0.22	0.23	0.20
MgO	0.83	12.65	11.65	10.45	12.15	12.60	12.20	9.57	10.40	7.90	8.01	9.56
CaO	0.39	14.60	13.05	14.30	12.55	12.55	13.20	14.05	11.95	14.50	13.85	11.85
Na_2O	1.14	0.54	1.08	1.24	0.83	1.06	1.06	1.32	1.54	2.25	1.84	1.93
K_2O	4.82	2.50	2.33	1.50	3.66	2.64	1.84	0.98	1.85	0.62	0.72	1.62
P_2O_5	0.09	0.32	0.40	0.39	0.36	0.33	0.38	0.39	0.38	0.40	0.37	0.38
Cr_2O_3	0.01	0.14	0.12	0.13	0.15	0.15	0.16	0.12	0.12	0.11	0.12	0.11
LOI	0.47	1.02	0.81	0.72	1.06	1.57	1.25	1.04	1.01	2.02	1.33	1.23
Total	100.72	100.72	99.92	99.28	99.47	99.55	99.66	99.15	99.59	100.10	100.00	99.86
Sc	7.80	42.5	42.9	43.3	38.5	38.8	40.0	42.3	40.1	38.3	40.3	38.3
V	34.4	402	409	424	369	374	398	413	390	379	403	384
Cr	55.40	794	683	751	875	926	944	743	697	639	712	661
Co	4.09	66.2	52.5	70.8	67.4	74.9	56.7	68.7	65.5	56.3	68.4	60.8
Ni	17.80	243	240	256	300	327	327	248	224	214	246	204
Cu	5.32	29.2	84.5	115	26.4	64.8	142	444	121	27.4	427	70.2
Rb	103	105	97.9	44.8	214	102	70.8	30.4	56.9	14.6	12.8	48.8
Sr	154	555	831	546	244	409	442	648	580	1040	973	731
Y	19.6	34.9	28.8	29.4	27.3	24.9	26.3	26.2	26.0	26.3	26.8	27.6
Zr	411	143	154	130	109	127	132	135	132	138	160	144
Nb	9.01	32.1	48.6	43.1	47.6	41.4	44.7	46.7	47.8	48.8	51.6	46.7
Ba	961	1360	421	1100	767	991	667	801	1030	1190	1110	994
La	28.4	69.1	47.6	43.6	39.3	55.2	43.0	44.9	51.8	48.4	51.9	51.0
Ce	58.1	141	117	110	101	117	107	111	120	114	122	116
Pr	6.33	18.0	16.6	16.0	14.0	15.3	15.4	15.9	16.4	15.6	16.4	15.7
Nd	23.4	75.4	71.3	70.5	62.4	64.8	68.1	67.5	69.9	67.9	70.8	66.7
Sm	4.33	14.0	13.3	13.0	11.2	11.6	12.1	12.8	12.5	12.1	12.4	12.3
Eu	1.09	3.93	3.97	4.06	3.52	3.66	3.70	4.14	3.98	3.97	4.10	4.05
Gd	4.39	12.3	11.5	11.8	10.1	10.3	10.7	11.0	11.1	10.8	11.1	10.7
Tb	0.65	1.52	1.36	1.45	1.28	1.20	1.35	1.36	1.38	1.28	1.34	1.27
Dy	3.41	7.32	6.76	6.80	5.93	5.78	6.25	6.29	6.40	6.01	6.48	6.35
Ho	0.74	1.39	1.26	1.20	1.16	1.06	1.15	1.17	1.13	1.10	1.16	1.17
Er	2.11	3.65	3.19	3.11	2.98	2.70	2.92	3.14	2.85	2.74	2.97	3.06
Tm	0.30	0.45	0.42	0.41	0.38	0.35	0.39	0.37	0.36	0.36	0.40	0.35
Yb	1.95	2.60	2.34	2.30	2.04	2.07	2.07	2.26	2.16	2.07	2.23	2.09
Lu	0.26	0.33	0.33	0.33	0.29	0.28	0.29	0.27	0.29	0.30	0.33	0.30
Hf	11.39	5.20	5.40	4.85	4.02	4.33	4.81	5.18	4.92	4.75	5.44	4.88
Ta	0.72	1.69	3.37	3.04	2.46	2.64	3.02	3.32	3.41	3.22	3.59	3.17
Pb	17.50	3.93	8.09	3.52	4.17	7.48	2.57	5.02	5.85	4.05	10.30	23.90
Th	13.80	3.60	1.05	0.58	0.44	1.10	0.13	0.41	0.49	1.45	0.56	0.26
U	1.65	2.54	0.33	0.51	0.91	0.91	0.06	0.07	0.11	0.28	0.14	0.06

Sample	HG 16	HG 16	HG17	HG18	HG19	HG20	HG22	HG26	BC1311	BC1312	BC1313	BCR-2	BCR-2
Rock type	gabbro	Duplicate	olivine gabbro	olivine gabbro	olivine gabbro	olivine gabbro	olivine gabbro	olivine gabbro	syenite	syenite	syenite	measured	accepted values
SiO_2	46.41	45.89	42.32	42.25	42.47	42.17	41.44	43.05	63.6	64.2	62.4	53.52	54.00
TiO_2	3.78	3.66	2.98	2.94	3.16	2.83	3.12	2.72	0.70	0.40	0.85	2.242	2.27
Al_2O_3	7.63	7.39	1.86	3.08	2.47	3.44	2.86	2.87	18.25	17.95	17.65	13.30	13.48
$Fe_2O_3^T$	14.12	14.03	13.56	14.04	13.59	13.44	14.36	13.59	3.14	2.67	4.13	13.65	13.77
MnO	0.19	0.19	0.19	0.20	0.23	0.16	0.20	0.20	0.10	0.09	0.13	0.198	0.20
MgO	10.65	11.68	23.5	23.8	23.6	23.5	23.0	23.9	0.09	0.29	0.46	3.57	3.60
CaO	12.15	11.72	9.35	8.55	8.58	7.03	8.68	9.93	0.32	0.64	1.12	6.91	7.11
Na_2O	1.92	2.07	0.32	0.25	0.25	0.18	0.27	0.47	7.09	7.12	6.74	3.16	3.12
K_2O	1.06	1.09	0.64	1.90	1.38	1.88	1.68	0.36	5.38	5.26	5.23	1.78	1.77
P_2O_5	0.37	0.326	0.29	0.32	0.50	0.35	0.31	0.30	0.08	0.06	0.18	0.345	0.36
Cr_2O_3	0.11	–	0.29	0.28	0.27	0.27	0.28	0.27	–	–	–	–	–
LOI	1.54	1.82	4.15	1.45	2.81	3.96	2.68	1.84	0.39	0.26	0.32	–	–
Total	100.11	99.87	99.87	99.50	99.75	99.55	99.68	99.72	99.14	98.94	99.21	98.68	99.68
Sc	37.8	32.7	27.2	24.1	25.3	20.8	21.4	19.3	8.56	8.56	8.06	33.8	33.5
V	358	357	279	249	245	221	217	204	7.44	1.79	11.9	379	418
Cr	630	645	1540	1450	1400	1330	1330	1240	7.46	1.84	3.32	17.1	15.9
Co	56.1	58.6	94.8	91.2	88.2	85.5	90.0	84.7	0.40	0.28	1.61	37.8	37.3
Ni	226	219	1060	1010	1030	948	933	933	1.64	1.06	3.90	14.3	12.6
Cu	32.7	33.6	92.2	112	176	49.9	270	17.8	5.07	3.13	8.00	25.1	19.7

(*continued on next page*)

Table 1 (*continued*)

Sample	HG 16	HG 16	HG17	HG18	HG19	HG20	HG22	HG26	BC1311	BC1312	BC1313	BCR-2	BCR-2
Rock type	gabbro	Duplicate	olivine gabbro	olivine gabbro	olivine gabbro	olivine gabbro	olivine gabbro	olivine gabbro	syenite	syenite	syenite	measured	accepted values
Rb	33.9	32.6	30.1	91.6	65.7	98.8	88.6	16.0	67.4	64.8	66.0	49.4	46.02
Sr	560	586	315	359	401	402	298	374	67.5	46.7	217	369	337
Y	27.8	28.2	16.4	15.7	18.4	15.9	14.7	15.8	4.95	5.41	12.7	34.3	36.1
Zr	117	115	100	78.2	85.0	67.3	79.4	103	26.7	25.8	53.6	189	187
Nb	41.6	46.5	27.2	28.0	27.2	21.7	28.5	25.8	13.1	9.56	19.0	12.4	12.4
Ba	713	695	464	672	977	632	518	253	801	896	3450	750	684
La	44.6	44.0	29.8	36.0	47.5	39.3	29.2	22.8	11.2	10.9	30.1	28.0	25.1
Ce	106	107	76.8	89.2	108	92.5	67.5	62.7	25.1	24.3	62.4	58.7	53.1
Pr	14.9	14.7	11.2	12.4	15.7	13.5	9.95	9.81	2.79	3.15	7.91	7.11	6.83
Nd	62.5	64.1	50.2	53.5	64.7	55.3	40.6	41.6	11.9	13.7	33.3	29.3	28.3
Sm	11.7	11.7	9.14	9.21	11.00	9.52	7.42	7.82	2.06	2.47	5.74	6.60	6.55
Eu	3.86	3.37	2.54	2.60	3.17	2.73	2.42	2.38	1.34	1.51	2.36	1.80	1.99
Gd	10.5	9.59	7.54	7.07	8.53	8.41	6.64	6.77	1.59	1.72	4.21	6.01	6.81
Tb	1.33	1.33	0.88	0.85	1.04	0.89	0.72	0.71	0.23	0.28	0.63	1.10	1.08
Dy	5.94	6.12	3.96	3.89	4.32	3.86	3.25	3.34	1.18	1.28	2.89	6.17	6.42
Ho	1.14	1.10	0.69	0.66	0.76	0.65	0.55	0.56	0.21	0.22	0.49	1.39	1.31
Er	2.88	3.03	1.62	1.50	1.82	1.60	1.38	1.31	0.54	0.56	1.29	3.68	3.67
Tm	0.36	0.36	0.19	0.18	0.21	0.18	0.16	0.15	0.06	0.07	0.15	0.52	0.53
Yb	2.02	2.19	1.04	1.03	1.18	1.04	0.93	0.90	0.40	0.46	0.89	3.33	3.39
Lu	0.28	0.30	0.13	0.12	0.15	0.15	0.13	0.12	0.06	0.08	0.13	0.48	0.50
Hf	4.26	4.15	3.55	2.58	2.52	2.39	2.41	3.63	0.71	0.68	1.51	5.04	4.97
Ta	2.76	3.14	2.03	1.77	1.63	1.18	1.82	1.63	0.71	0.56	1.04	0.81	0.79
Pb	4.65	4.73	2.67	6.12	9.51	3.28	3.65	10.10	3.58	2.96	4.98	11.3	10.6
Th	0.29	0.29	0.67	0.30	0.73	0.33	0.79	0.36	0.66	0.78	1.90	6.06	5.83
U	0.05	0.11	0.13	0.16	0.16	0.06	0.45	0.10	0.14	0.17	0.40	1.78	1.68

Note: LOI: loss on ignition. The accepted values of BCR-2 are from Jochum et al. (2016).

isotopic compositions are more enriched than those of the overlying layered series (Luan et al., 2014), spatially associated syenites (Wang et al., 2013, 2015), and basalts (Liao et al., 2015), and represent the most enriched endmember of high-Ti basaltic series observed in the ELIP to date (Fig. 6a). In general, the ε_{Nd} values of the marginal rocks and overlying basalts are positively correlated with their SiO_2 contents and Hf/Nd ratios (Fig. 5c-d). The marginal zone rocks have ε_{Hf} values of −2.37 to −6.01 (Fig. 7a). These values are more enriched than those from the layered cumulate series and the spatially and temporally associated felsic rocks (Fig. 7a). It is worth noting that the marginal zone rocks plot above the terrestrial array defined by Vervoort et al. (2011) on an ε_{Hf} versus ε_{Nd} diagram (Fig. 7a). Similar decoupling between the Nd and Hf isotopic compositions is observed in other mafic and felsic intrusions in the ELIP. The footwall sedimentary rocks are characterized by enriched Nd—Hf isotopic compositions ($\varepsilon_{Nd(t)} = -13.74$, $\varepsilon_{Hf(t)} = -15.78$) and high initial $^{87}Sr/^{86}Sr$ (0.718887), similar to those of typical Yangtze upper crust (Chen and Jahn, 1998).

4.3. Zircon Hf—O isotopic compositions of the syenite

The zircon Hf—O isotopic compositions of the Hongge syenite are listed in Table 3. All of the zircon grains are bright and have magmatic oscillatory zoning in cathodoluminescence (CL) images (Fig. 7b). The syenites have zircon ε_{Hf} values of +3.7 to +6.6 (mean = +4.7), which overlap with the values of the layered series of the Hongge intrusion (Fig. 7b). These values are more depleted than those of the marginal zone rocks but more enriched than those of other mafic and felsic intrusions in the ELIP. The zircon grains from the syenite samples yield $\delta^{18}O$ values of 3.9–5.7‰, which overlap with those of mantle zircon (5.3 ± 0.3‰; Valley, 2003) and extend to lower values. Similar low zircon $\delta^{18}O$ values have been observed in the Taihe mafic–ultramafic intrusion in the ELIP (Tang et al., 2021).

5. Discussion

5.1. Source or process control on magma compositions?

The fine-grained equigranular textures of the Hongge marginal gabbros (Fig. 2b) are consistent with the rapid nucleation and cooling processes that differ from coarse-grained cumulus gabbros. Cumulus gabbros also have significantly lower contents of incompatible elements (e.g. HFSE and REEs) compared to the coeval basalts in ELIP (e.g. Pang et al., 2010). Combining this observation with the undepleted incompatible element contents of these marginal samples (Fig. 4), we suggest that these rocks represent rapidly solidified Emeishan high-Ti basaltic magma (e.g. Xu et al., 2001) that was quenched during emplacement along the floor of the magma chamber. The absence of Eu anomaly in the marginal rocks (Fig. 4a) is consistent with the interpretation that these marginal gabbros are solidified magmas rather than cumulates formed from the Emeishan high-Ti basaltic magma.

The most notable compositional features of the Hongge marginal rocks, spatially associated basalts, and syenites are the depletion of Zr and Hf contents (Fig. 4b), enrichment of Sr—Nd isotopic compositions (Fig. 6) and the decoupling of Nd—Hf isotopic compositions (Fig. 7a) from the Terrestrial Array (Vervoort et al., 2011). Recently, melt inclusions with weak negative Zr—Hf anomalies have also been found in the Lijiang picrites of the ELIP (Fig. 4b; Zhang et al., 2021). Mantle-derived magma can be modified by low-pressure magmatic processes, including fractional crystallization and crustal contamination, on its way to shallow crustal levels; therefore, the effects of these processes on the compositions of the Hongge magmas need to be evaluated. The marginal rocks and overlying basalts have much lower MgO contents than those of the primary magma (20–23% MgO; Hanski et al., 2010, Ren et al., 2017) for the ELIP. This implies that the parental magma of the marginal rocks has undergone abundant olivine, clinopyroxene, and probably plagioclase and Fe—Ti oxide crystallization. The variations in the major and trace element contents of the Hongge marginal rocks, coeval basalts, and syenites versus their MgO contents (Fig. 3) are consistent with the scenario that the magma composition was controlled by the fractional crystallization of these minerals. Zr/Sm and Hf/Nd ratios of the marginal rocks and overlying basalts increase with the decrease of MgO and increase of SiO_2 (Fig. 5b). It seems that the variations of these ratios were also caused by fractional crystallization. Zirconium, Hf, Sm, and Nd are highly incompatible in olivine and plagioclase (Aigner-Torres et al., 2007; Bédard, 2005). Therefore, the fractionation of olivine and plagioclase does not significantly change the

Table 2
Sr, Nd, Hf isotopic compositions of the marginal zone of the Hongge intrusions in ELIP.

sample	Rock type	$^{87}Rb/^{86}Sr$	$^{87}Sr/^{86}Sr$	±2σ	$(^{87}Sr/^{86}Sr)_t$	$^{147}Sm/^{144}Nd$	$^{143}Nd/^{144}Nd$	±2σ	$\varepsilon_{Nd}(t)$	$^{176}Lu/^{177}Hf$	$^{176}Hf/^{177}Hf$	±2σ	$\varepsilon_{Hf}(t)$
HG01	wall-rock	3.058896	0.730158	0.000008	0.718887	0.111858	0.511790	0.000007	−13.74	0.004018	0.282184	0.000004	−15.78
HG01	Duplicate										0.282190	0.000005	−15.57
HG05	gabbro	0.340471	0.710224	0.000018	0.708969	0.112761	0.512195	0.000007	−5.87	0.010587	0.282547	0.000005	−4.07
HG05	Duplicate										0.282544	0.000004	−4.17
HG11	gabbro	0.135580	0.709051	0.000017	0.708551	0.114631	0.512199	0.000007	−5.85	0.008974	0.282535	0.000004	−4.21
HG12	gabbro	0.283519	0.709411	0.000012	0.708366	0.108101	0.512180	0.000009	−6.01	0.010372	0.282594	0.000005	−2.37
HG15	gabbro	0.192930	0.709717	0.000008	0.709006	0.111475	0.512148	0.000007	−6.75	0.010809	0.282545	0.000004	−4.18
HG16	gabbro	0.174948	0.709528	0.000011	0.708883	0.113162	0.512147	0.000010	−6.81	0.011455	0.282547	0.000004	−4.22
HG17	olivine gabbro	0.276156	0.709810	0.000013	0.708792	0.110062	0.512121	0.000009	−7.23	0.006561	0.28247	0.000005	−6.10
HG18	olivine gabbro	0.737393	0.711433	0.000008	0.708716	0.104064	0.512105	0.000009	−7.33	0.008282	0.282478	0.000005	−6.11
HG20	olivine gabbro	0.710279	0.711265	0.000017	0.708648	0.104066	0.512086	0.000010	−7.70	0.010950	0.282494	0.000005	−6.01
HG22	olivine gabbro	0.859242	0.712776	0.000026	0.709610	0.110478	0.512099	0.000008	−7.67	0.009310	0.282491	0.000004	−5.83
BCR-2	measured		0.704990				0.512601				0.282864	0.000004	
BCR-2	accepted value		0.704920				0.512635				0.282865	0.000013	
BHVO-2	measured										0.283115	0.000004	
BHVO-2	accepted value										0.283082	0.000133	

The accepted values for reference materials are from http://georem.mpch-mainz.gwdg.de. $(^{87}Sr/^{86}Sr)_t$, $\varepsilon_{Nd}(t)$, $\varepsilon_{Hf}(t)$ were calculated to 260 Ma.
ε_{Nd} values were calculated using $(^{147}Sm/^{144}Nd)_{CHUR(0)} = 0.1967$ and $(^{143}Nd/^{144}Nd)_{CHUR(0)} = 0.512638$. ε_{Nd} values were calculated using $(^{176}Lu/^{177}Hf)_{CHUR(0)} = 0.0332$ and $(^{176}Hf/^{177}Hf)_{CHUR\ (0)} = 0.282772$.

Zr/Sm and Hf/Nd ratios of the magma. The fractionation of a large amount of Fe—Ti oxides should lead to depletion in Zr and Hf contents relative to Sm and Nd contents in the melt, since Zr and Hf are less incompatible than Sm and Nd in magnetite and ilmenite (e.g. Klemme et al., 2006). The marginal rocks have the lowest SiO_2 and highest MgO content as well as the lowest Zr/Sm and Hf/Nd ratios (Fig. 5b). However, the high FeO_T and TiO_2 contents of most of the marginal rocks indicate negligible Fe—Ti oxide fractionation from these rocks. Therefore, the marked depletion of Zr and Hf contents in the marginal rocks was not caused by the fractionation of Fe—Ti oxides. On the other hand, the decrease of FeO_T and TiO_2 contents with the decrease of MgO and the increase of SiO_2 in the marginal rocks and overlying basalts may be consistent with the fractionation effect of Fe—Ti oxides (Fig. 4). However, the increase of Zr/Sm and Hf/Nd ratios with the decrease of MgO and the increase of SiO_2 (Fig. 5b) also cannot be explained by the fractionation of Fe—Ti oxides, since the fractionation of Fe—Ti oxide would decrease these ratios. Zirconium, Hf, Sm, and Nd are moderately incompatible in clinopyroxene. In addition, the incompatibility of Sm and Nd in clinopyroxene is less than Zr and Hf (Hart and Dunn, 1993; Hauri et al., 1994). Consequently, the Zr/Sm and Hf/Nd ratios of the magma would gradually increase with the clinopyroxene fractionation. This means that the marked depletion of Zr and Hf contents in the marginal rocks was not caused by clinopyroxene fractionation (Figs. 4 and 5). A simple Rayleigh fractionation model using the partition coefficients between clinopyroxene and basaltic magma (Hauri et al., 1994) shows that after 50% fractional crystallization of clinopyroxene, the Zr/Sm and Hf/Nd ratios can only increase by 20% and 4%, respectively. With the increase of SiO_2 content, Zr/Sm and Hf/Nd ratios increased from 7.1 and 0.04 in marginal rocks to 38.3 and 0.13 in overlying basalts, respectively (Fig. 5b). Such remarkable increases of Zr/Sm and Hf/Nd ratios are difficult to reconcile with the model of clinopyroxene fractionation. In conclusion, the marked depletion of Zr and Hf contents and large variations in Zr/Sm and Hf/Nd ratios in these rocks were not mainly caused by fractional crystallization.

The enriched Sr—Nd isotopic compositions of the marginal rocks may be explained by contamination of upper crustal material (e.g. wall rocks) during ascent to shallow levels. However, a mass balance calculation for mixing between the most depleted Emeishan basalt and the upper crust shows that reducing the ε_{Nd} value from +3 in depleted Emeishan magma (Chung and Jahn, 1995) to about −7 in these rocks requires an addition of 60%–70% crustal material (Fig. 6a). Such a high extent of crustal contamination cannot be attained with reasonable heat budgets. Moreover, after the incorporation of such large amounts of crustal material, the mixed magma would have an intermediate composition with low FeO_T and TiO_2 contents rather than Fe- and Ti-rich mafic compositions (Figs. 6b). EC-AFC (Spera and Bohrson, 2001) modeling was employed to test the possibility of such enriched isotopic compositions acquired by crustal contamination (Fig. 6a). The results show that the picritic magma with an initial liquid temperature of 1450 °C would only contaminate <40% of upper crustal material during the temperature fall to the equilibration temperature of 1200 °C (liquid temperature of marginal rocks). The calculated isotopic composition of the contaminated magma is significantly depleted than these of the marginal rocks. Thus, the enriched Sr—Nd isotopic compositions of the marginal rocks cannot be explained by crustal contamination. Other geochemical arguments against crustal contamination include the absence of a positive correlation between $^{87}Sr/^{86}Sr$ ratios and 1/Sr contents, and negative Zr—Hf anomalies (Fig. 4b). In particular, the remarkably low Zr/Sm and Hf/Nd ratios (Fig. 5c–d) cannot be reconciled with upper-crust contamination because the Zr/Sm (~37) and Hf/Nd (~0.17) ratios of the Yangtze upper crust (Gao et al., 1998) are close to those of the depleted Emeishan basalts (Hf/Nd = 0.15; (Xu et al., 2001)). In fact, the wall-rocks of the Hongge intrusion have positive Zr—Hf anomalies relative to Nd and Sm (Fig. 4b). In addition, mixing between two endmembers with similar Hf/Nd ratios cannot decouple the Nd and Hf isotopic compositions (Fig. 7a).

Table 3
Zircon Lu—Hf and O isotopic compositions for the syenite associated with the Hongge intrusion in ELIP.

Spot	$^{176}Yb/^{177}Hf$	$^{176}Lu/^{177}Hf$	$^{176}Hf/^{177}Hf$	1σ	$\varepsilon_{Hf}(t)_a$	$\delta^{18}O$	2σ
BC1311-01	0.025916	0.000794	0.282763	0.000020	5.3	4.66	0.27
BC1311-02	0.016209	0.000477	0.282743	0.000018	4.6	4.34	0.41
BC1311-03	0.026880	0.000772	0.282737	0.000018	4.3	4.80	0.27
BC1311-04	0.020603	0.000602	0.282753	0.000021	4.9	5.25	0.29
BC1311-05	0.015898	0.000540	0.282726	0.000019	4.0	5.41	0.35
BC1311-06	0.013435	0.000433	0.282727	0.000017	4.0	5.09	0.26
BC1311-07	0.018572	0.000600	0.282770	0.000022	5.5	5.11	0.28
BC1311-08	0.032256	0.000961	0.282743	0.000020	4.5	4.86	0.28
BC1311-09	0.032428	0.001101	0.282756	0.000022	5.0	3.94	0.31
BC1311-10	0.015780	0.000506	0.282725	0.000022	4.0	4.66	0.33
BC1311-11	0.032684	0.001049	0.282730	0.000022	4.0	4.91	0.36
BC1311-12	0.018418	0.000660	0.282738	0.000026	4.4	5.50	0.33
BC1311-13	0.054059	0.001753	0.282795	0.000029	6.2	5.68	0.47
BC1311-14	0.021953	0.000723	0.282747	0.000022	4.7	4.58	0.43
BC1311-15	0.021613	0.000697	0.282718	0.000022	3.7	5.67	0.52
BC1311-16	0.015957	0.000529	0.282747	0.000022	4.7	5.15	0.57
BC1311-17	0.030112	0.000958	0.282801	0.000022	6.6	4.17	0.30
BC1311-18	0.014418	0.000478	0.282738	0.000024	4.4	4.84	0.26
BC1311-19	0.019417	0.000595	0.282736	0.000023	4.3	4.85	0.31
BC1311-20	0.024895	0.000732	0.282748	0.000023	4.8	4.57	0.32
Measured values for reference materials							
91500	0.011150	0.000302	0.282304	0.000017			
GJ-1	0.010538	0.000293	0.282013	0.000016			
Plešovice	0.006136	0.000114	0.282471	0.000014			
Mud Tank	0.002829	0.000062	0.282507	0.000014			
Penglai	0.019944	0.000467	0.282914	0.000016		5.27	0.30
Qinghu						5.41	0.28
Accepted values for reference materials							
91500 (Wu et al., 2006)			0.282307	0.000031			
GJ-1 (Morel et al., 2008)			0.282000	0.000005			
Plešovice (Sláma et al., 2008)			0.282482	0.000013			
Mud Tank (Gain et al., 2019)			0.282523	0.000010			
Penglai (Li et al., 2010)			0.282906	0.000016		5.31	0.10
Qinghu (Li et al., 2013)						5.40	0.20

a. $\varepsilon_{Hf}(t)$ were calculated to $t = 260$ Ma.

Compared with the marginal rocks, the overlying basalts have more depleted ε_{Nd} values and relatively high Zr/Sm, Hf/Nd ratios, and SiO_2 contents (Fig. 5c-d). Overall, the Zr/Sm, Hf/Nd ratios and SiO_2 contents of the marginal rocks and overlying basalts show positive correlations with their ε_{Nd} values. Such variation trends are also difficult to reconcile with the model of crustal contamination, since a magma parental to the marginal rocks contaminated by upper crustal material would show negative correlations between ε_{Nd} values and Zr/Sm and Hf/Nd ratios. It has been demonstrated that magmas in the ELIP with large compositional diversity were generated by the mixing of magma with different compositions in a deep magma chamber (Ren et al., 2017). Therefore, the linear trends (Fig. 5b-d) can be attributed to the mixing of a magma with enriched ε_{Nd} values and depleted Zr—Hf content (e.g. parental magma of the marginal rocks) and an evolved magma (low MgO and high SiO_2) with relative depleted ε_{Nd} values and undepleted Zr—Hf contents (e.g. evolved Emeishan basalt).

In summary, the available data indicate that the geochemical and isotopic characteristics of these marginal rocks were not mainly caused by crustal magmatic processes such as fractional crystallization and crustal contamination. We suggest that these unusual geochemical characteristics were inherited from the mantle source.

5.2. Recycled oceanic sediment and altered crust in the mantle source

The enriched Sr—Nd isotopic compositions of these marginal rocks indicate that upper crustal material was an important source component of their parental magma. Enriched chemical and isotopic signatures have occasionally been found in ocean island basalts, where they are thought to result from an influx of oceanic crust and overlying sediment into the mantle source through subduction (Hofmann and White, 1982; Jackson et al., 2007; White and Hofmann, 1982). Consequently, the mixing of subducted material with mantle peridotite in the deep mantle is likely to have produced the crustal signatures in some of the ELIP samples, as shallow crustal contamination can be ruled out. Marine sediments are derived mainly from the upper continental crust and thus introduce a continental signature to the mantle.

Zircon is the main Zr and Hf reservoir in the upper continental crust and is highly resistant to chemical alternation. As a result, most of the Zr and Hf is sequestered in zircon grains during weathering, and these grains are preferentially sorted into sand on the continents and continental shelves (Patchett et al., 1984). In contrast, more easily altered rock-forming minerals commonly have Zr/REE and Hf/REE ratios that are lower than those of resistant minerals (Bayon et al., 2006). Incongruent weathering of the crust leads to the depletion of Zr and Hf contents relative to REE contents in most terrigenous oceanic sediments. For example, Zr/Sm and Hf/Nd ratios are as low as 3.5 and 0.02, respectively, in marine sediments (Plank and Langmuir, 1998), which are much lower than the ratios in the primitive mantle (McDonough and Sun, 1995), OIB (Sun and McDonough, 1989), and Yangtze upper crust (Gao et al., 1998; Fig. 5). The low Zr/Sm and Hf/Nd ratios and positive correlation between Nd isotopic compositions and Hf/Nd ratios in the samples of the Hongge marginal rocks and spatially associated basalts are consistent with the incorporation of marine sediments with low Zr/REE and Hf/REE ratios in their mantle source (Fig. 5a). The Nd isotopic compositions of the marine sediments are probably similar to those of sediment from the South and East China seas (Li et al., 2003; Saitoh et al., 2015) and the average upper crust of China (Chauvel et al., 2014). The Hf/Nd ratio of the marine sediments, estimated using the positive correlation between Nd isotopic compositions and Hf/Nd ratios in the ELIP samples (Fig. 5d), is about 0.05, which is within the range of global marine sediments reported by Plank and Langmuir (1998). Mixing models for the source indicate that the addition of ~10% and <3% marine sediment to the mantle can explain the Sr—Nd isotopic composition of these early-formed rocks from the marginal zone and overlying

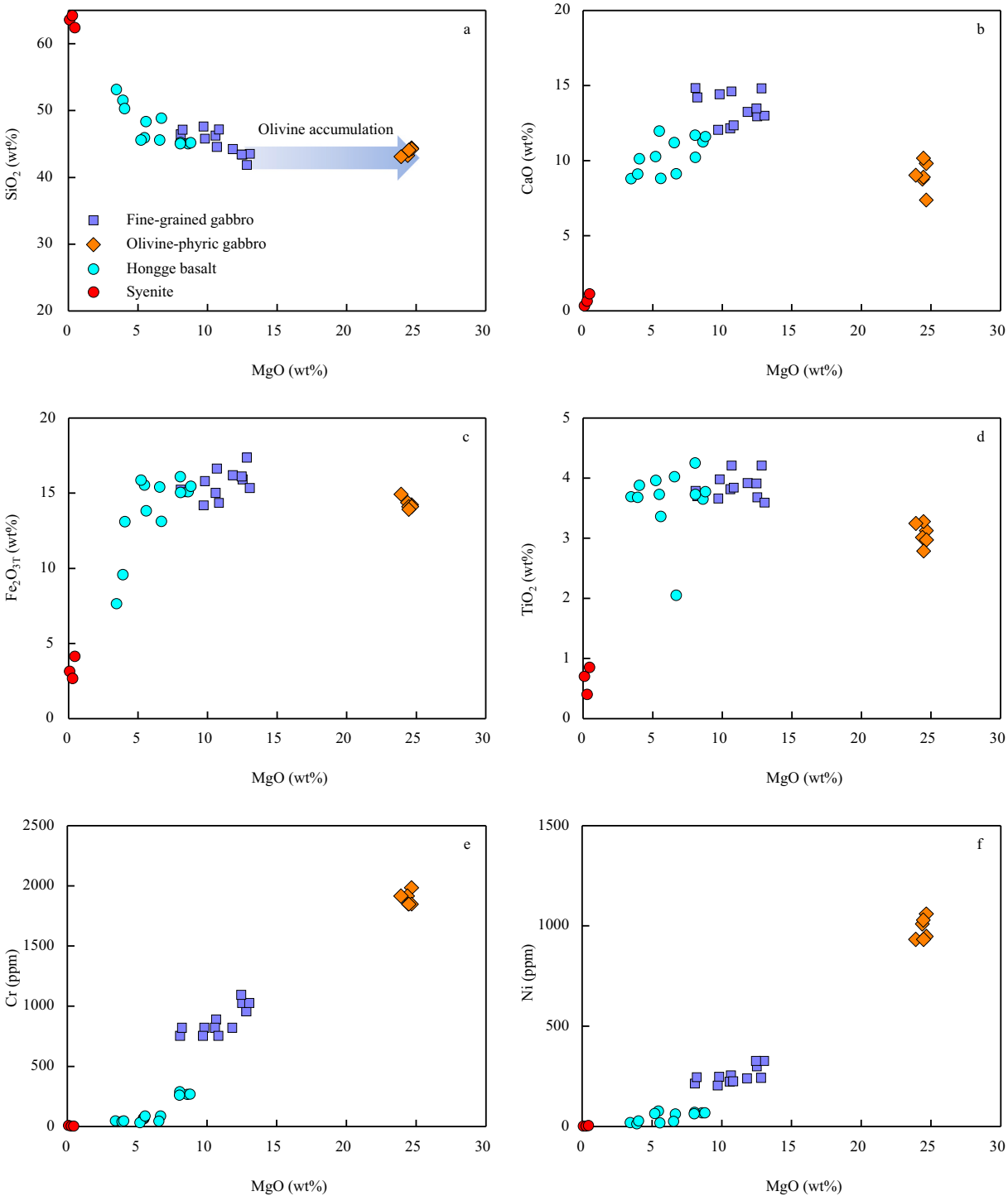

Fig. 3. Whole-rock (a) SiO_2, (b) CaO, (c) Fe_2O_{3T}, (d) TiO_2, (e) Cr, and (f) Ni contents versus MgO contents of the marginal rocks of the Hongge intrusion and the overlying basalt and syenite.

later-formed layered series of the Hongge intrusion, respectively (Fig. 6a). Mixing of a variable amount of marine sediments with low Hf/Nd ratios (~0.05) and mantle peridotite (Hf/Nd = ~0.23) also accounts for the decoupling of Nd and Hf isotopic compositions in these samples as well as in other mafic–felsic intrusions of the ELIP (Fig. 7a). The marine sediments are more fusible than mantle peridotites and subducted oceanic crusts. Therefore, the signal of marine sediments is more robust in the magma generated in the early stage and decreases in the magma generated in the late stage during partial melting. This may be the reason for the lack of obvious negative Zr—Hf anomalies and enriched Sr-Nd-Hf isotope compositions in most Emeishan basalts and picrites that were generated in the late stage.

The Sr–Nd–Hf isotopic compositions of the Hongge syenites (Wang et al., 2013, 2015) are similar to those of the layered series of the Hongge intrusion, suggesting that they were derived from a common parental magma. The overlap of isotopic compositions between the mafic-ultramafic intrusions and spatially associated syenites / A-type granites also occurs in other mafic–felsic intrusive associations of the ELIP (Fig. 7a; Shellnutt et al., 2009a, 2009b, 2011; Zhong et al., 2011; Song et al., 2013). However, there are significant differences between

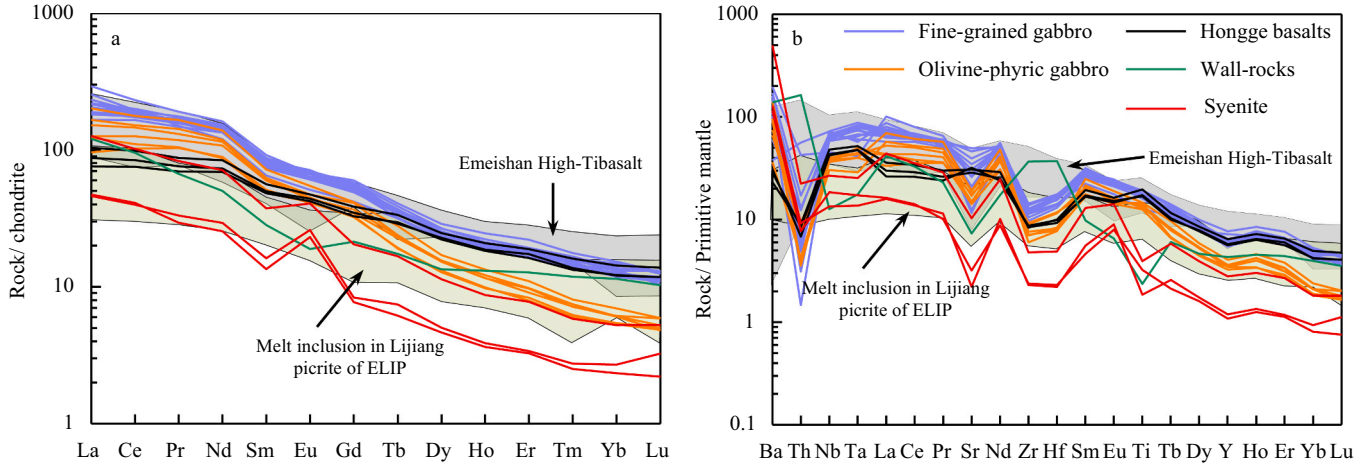

Fig. 4. (a) Chondrite-normalized REE patterns and (b) primitive-mantle-normalized alteration-resistant trace element patterns of the wall rock and marginal rocks of the Hongge intrusion and overlying basalt and syenite. The chondrite and primitive mantle compositions are from Sun and McDonough (1989) and McDonough and Sun (1995), respectively. The fields for the Emeishan high-Ti basalts and melt inclusion in Lijiang picrite are based on the data from Xu et al. (2001), Xiao et al. (2004) and Zhang et al. (2021).

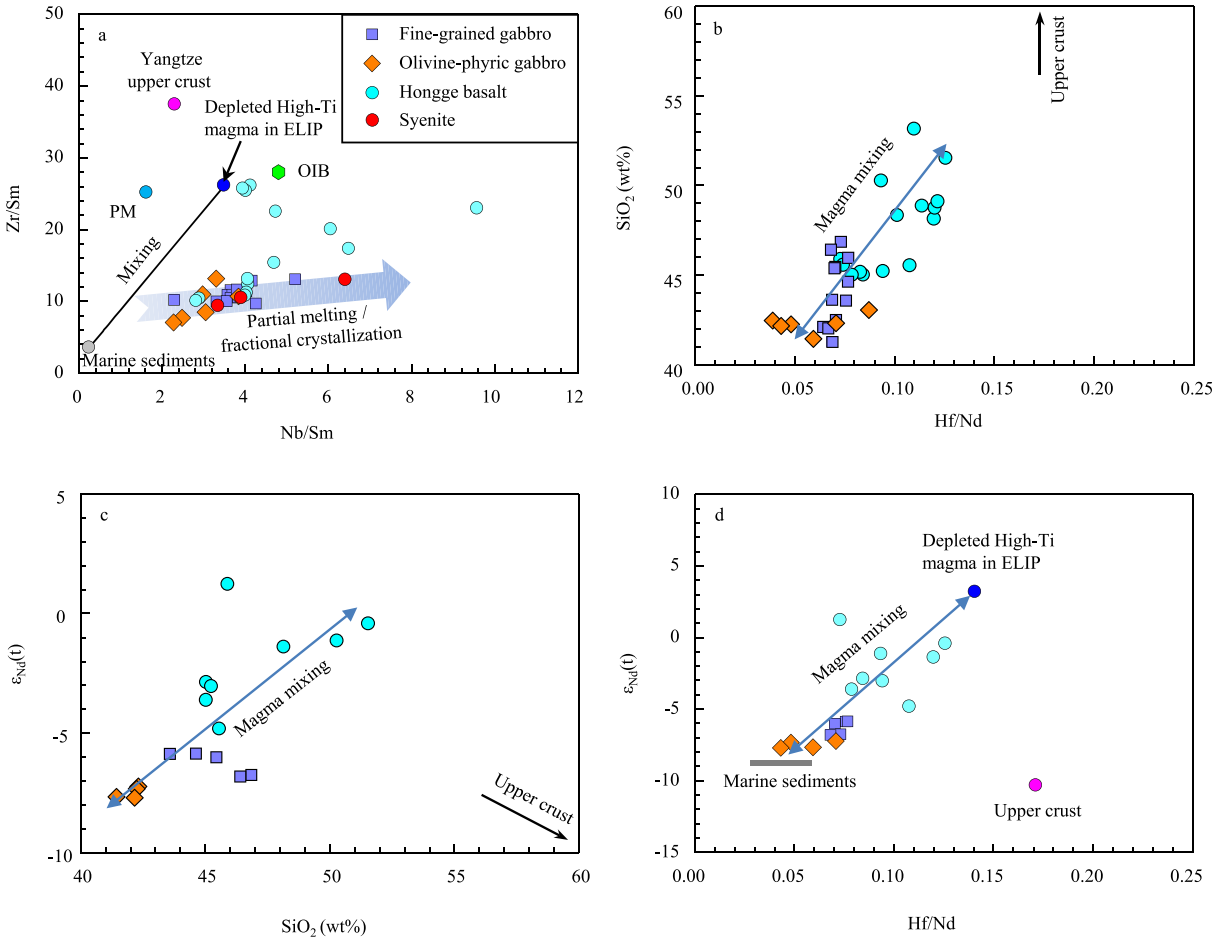

Fig. 5. (a) Zr/Sm versus Nb/Sm, (b) SiO_2 versus Hf/Nd, (c) ε_{Nd} values versus SiO_2, and (d) ε_{Nd} values versus Hf/Nd ratio of the rocks of the marginal zone of the Hongge intrusion and overlying basalt and syenite. Data for primitive mantle (McDonough and Sun, 1995), OIB (Sun and McDonough, 1989), and Yangtze upper crust (Gao et al., 1998) are shown for comparison. The data for the Hongge basalt are from Liao et al. (2015). The Zr/Sm and Nb/Sm ratios of marine sediments are from Plank and Langmuir (1998), and the ε_{Nd} value of marine sediments is that of sediments from the South and East China seas (Li et al., 2003; Saitoh et al., 2015) and the average composition of the upper crust of China (Chauvel et al., 2014).

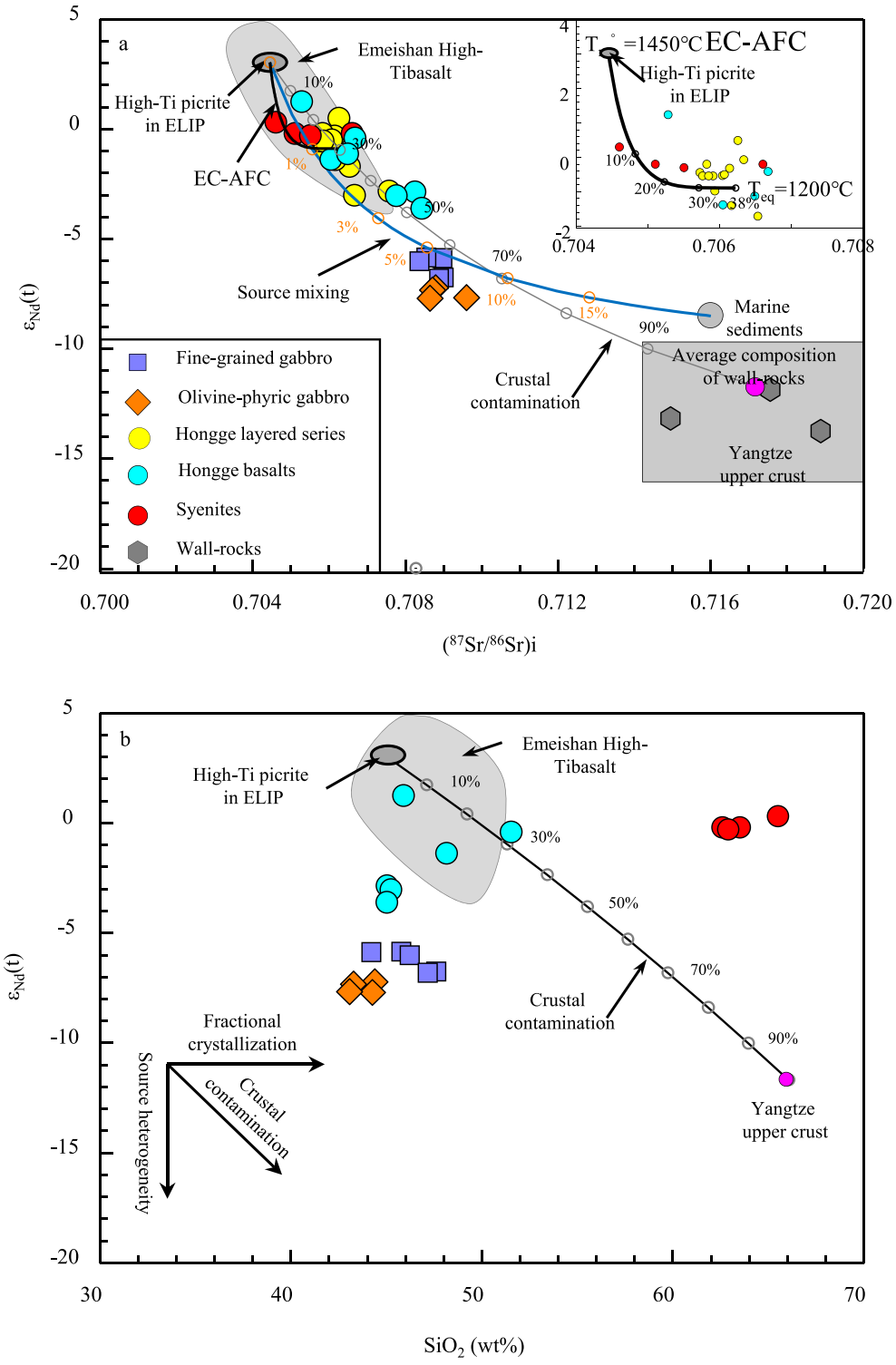

Fig. 6. ε_{Nd} value versus (a) $^{87}Sr/^{86}Sr$ ratios and (b) SiO_2 content for the Hongge intrusion and overlying basalt and syenite. The uncertainty is smaller than the symbols. Data for the Hongge basalt are from Liao et al. (2015), for the wall rocks and layered zone of the Hongge intrusion are from Luan et al. (2014), for the syenites are from Wang et al. (2013, 2015). The field for the Emeishan high-Ti basalts is based on the data from Xu et al. (2001), Xiao et al. (2004) and Zhang et al. (2008). The Sr and Nd content Sr and Nd isotope compositions of the depleted high-Ti magma (444 ppm Sr, 30 ppm Nd) and mantle peridotite (21 ppm Sr, 1.35 ppm Nd) in the ELIP are from Chung and Jahn, 1995 and Sun and McDonough (1989), respectively. The Sr and Nd content Sr and Nd isotope compositions of upper crust (175 ppm Sr, 26 ppm Nd) are from Gao et al. (1998, 1999) and Chen and Jahn (1998), and marine sediments (222 ppm Sr, 70 ppm Nd) are from Chauvel et al. (2014), Li et al. (2003), Plank and Langmuir (1998) and Saitoh et al. (2015). The EC-AFC modeling are from Spera and Bohrson (2001).

different mafic–felsic associations. For example, the Sr–Nd–Hf isotopic compositions of the Panzhihua and Taihe mafic–felsic intrusions are remarkably more depleted than those of the Hongge mafic–felsic intrusions. These characteristics imply that the felsic intrusions were produced by fractional crystallization from the high-Ti basaltic magma, representing the residual melts of the crystallization of the spatially associated mafic–ultramafic intrusions.

Zircon grains in the Hongge syenite have $\delta^{18}O$ values of 3.9‰–5.7‰ (Fig. 7b), with more than half yielding $\delta^{18}O$ values lower than those of zircon in equilibrium with mantle-derived magmas (5.3 ± 0.3‰; Valley, 2003). The zircons yield $\varepsilon_{Hf}(t)$ values of 3.7–6.6, close to those of the coarse-grained Hongge gabbro but much higher than those of the Hongge marginal rocks. The zircon grains are bright in CL images and show magmatic oscillatory zonation (Fig. 7b), suggesting that they were not altered by post-magmatic hydrothermal fluids or damaged by radiation and thus record initial magmatic $\delta^{18}O$ values. Similar zircon grains, and clinopyroxene with low $\delta^{18}O$ and high $\varepsilon_{Hf}(t)$ values have been observed in the Panzhihua and Taihe gabbros from this area

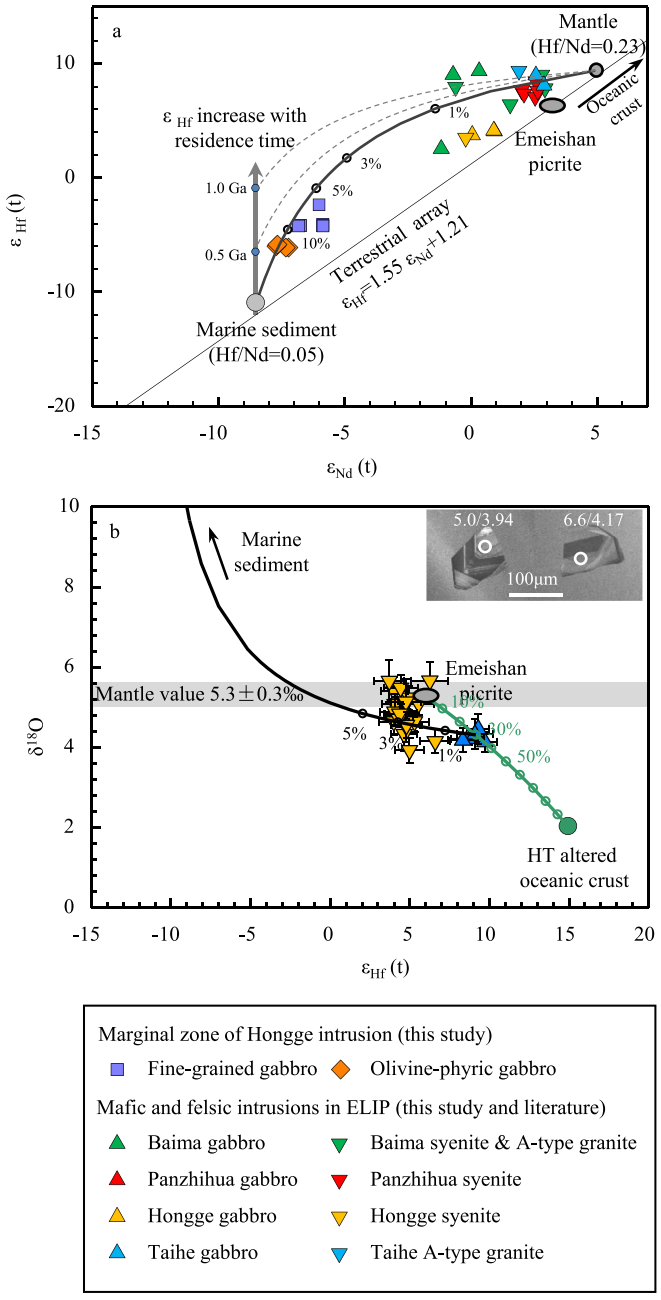

Fig. 7. (a) ε_{Hf} versus ε_{Nd} values and (b) $\delta^{18}O$ versus ε_{Hf} values for the Hongge intrusion and other mafic and felsic intrusion in the ELIP. The uncertainty in panel a is smaller than the symbols. Cathodoluminescence (CL) images of representative zircon grains with their Hf/O isotope compositions are shown in the inset in (b); circles indicate the sites of Hf—O isotopic analyses. The $\delta^{18}O$ value of mantle zircon is from Valley (2003); the compositions of mafic–felsic intrusions are from Shellnutt et al. (2009a, 2009b, 2011), Tang et al. (2021), Wang et al. (2013, 2015), and Zhong et al. (2011); the composition of primitive mantle is from McDonough and Sun (1995); the composition of marine sediments is from Li et al. (2003), Saitoh et al. (2015), and Chauvel et al. (2014); and the composition of oceanic crust altered at high temperatures is from Eiler (2001), and Zindler and Hart (1986).

(Zhang et al., 2009; Tang et al., 2021) and in the A-type granites from southeast of the ELIP (Xu et al., 2021). This unusual Hf—O composition cannot be explained by low-pressure magmatic processes such as crustal contamination, as the upper crust commonly has elevated $\delta^{18}O$ and enriched $\varepsilon_{Hf}(t)$ values relative to mantle-derived magma. It was reported that Zircons from the Neoproterozoic granites in this area commonly have low $\delta^{18}O$ values (e.g. Zou et al., 2021). However, these rocks also have low $\varepsilon_{Hf}(t)$ values at ~260 Ma due to radiogenic growth through time. Therefore, the mantle-derived magma contaminated by these rocks would not have such high $\varepsilon_{Hf}(t)$ values as recorded in the Hongge and Taihe zircons (Tang et al., 2021). In fact, the low $\delta^{18}O$ and high $\varepsilon_{Hf}(t)$ values of the zircon in the gabbro and syenite in the ELIP suggest that a component with low $\delta^{18}O$ and depleted $\varepsilon_{Hf}(t)$ values has been added to the mantle source. The best candidate for this component is gabbroic rocks in the lower oceanic crust that have undergone high-temperature alteration, as such rocks commonly have lower $\delta^{18}O$ values than the mantle (Eiler, 2001) and MORB-like depleted $\varepsilon_{Hf}(t)$ values (Zindler and Hart, 1986). Our mixing model suggests that the amount of recycled oceanic crust was up to 30% (Fig. 7b).

5.3. Interaction between a mantle plume and a subducting oceanic slab

It has long been proposed that the enriched geochemical characteristics of OIB are inherited from ancient recycled oceanic crust and sediment that had been transported to the core–mantle boundary by subduction and then returned to the surface via a mantle plume (Eiler et al., 1997; Hofmann and White, 1982; Jackson et al., 2007). It has also been suggested that ancient recycled oceanic crust and its secondary products (pyroxenite) were involved in the genesis of the magmatism in the ELIP (Hou et al., 2011; Ren et al., 2017; Yu et al., 2017). For example, Ren et al. (2017) suggested that the Emeishan basalts were derived from a pyroxenite source that was the product of mixing of a recycled ancient (>2–1 Ga) oceanic crust component with a peridotite component from the lower mantle. Other studies have proposed that the enriched geochemical characteristics of the ELIP were generated by a mantle plume interacting with metasomatized continental lithospheric mantle that was modified by an ancient oceanic slab during Neoproterozoic subduction (~860–760 Ma; Hou et al., 2011; Yu et al., 2017). Two subduction events have been identified along the western margin of the Yangtze Block. In addition to Neoproterozoic subduction, the East Paleo-Tethyan oceanic plate was subducted eastward into the upper mantle beneath the Yangtze block during the late Carboniferous–Early Triassic (Metcalfe, 2013; Wang et al., 2018; Zhao et al., 2018).

As noted above, decoupling of the Nd—Hf isotopic compositions in the mafic–felsic intrusions in the ELIP requires the incorporation of marine sediments with low Hf/REE ratios (e.g. Hf/Nd = 0.05) in their mantle source. Marine sediments commonly deviate from the Terrestrial Array towards higher ε_{Hf} values at a given ε_{Nd} value due to their high Lu/Hf ratios caused by incongruent weathering (Bayon et al., 2006). The degree of Hf isotopic fractionation depends on the age of the crustal protolith, as the accumulation of radiogenic ^{176}Hf due to the decay of ^{176}Lu is time-dependent (Fig. 7a); therefore, marine sediment from an ancient protolith would have a more radiogenic ε_{Hf} value at a given ε_{Nd} value. As shown in Fig. 7a, the enriched Hf—Nd isotopic compositions and low Hf/Nd ratios of the marginal zone rocks require that the marine sediment component has a Hf isotopic composition that does not deviate far from the Terrestrial Array. This, together with the high Lu/Hf ratios of the marine sediments (inferred from the low Hf/Nd ratios of the marginal zone rocks), indicates that the marine sediments were derived from a juvenile rather than ancient crustal protolith, and also had a relatively short residence time in the mantle. The marine sediment is, therefore, more likely to have been introduced to the mantle during a subduction event shortly before the major melting event of the ELIP rather than during subduction in the Neoproterozoic or earlier (Fig. 7a). The slab that was subducted during the Neoproterozoic may have sunk into the lower mantle instead of remaining in the upper mantle beneath the western margin of the Yangtze block until 260 Ma, meaning that the Neoproterozoic slab is less likely have been involved in the Emeishan mantle plume.

This interpretation is also supported by the low $\delta^{18}O$ values of the parental magma of the mafic–felsic intrusions in the ELIP (Fig. 7b).

Oxygen isotope re-equilibration could have occurred after the low-$\delta^{18}O$ slab had been subducted into the mantle, which would have shifted the slab's $\delta^{18}O$ values towards normal mantle values. The transport rate for O is estimated to be 1000–2000 m/Ma at mantle temperatures and pressures (Zheng et al., 1998), meaning that a slab that was subducted during the Neoproterozoic or earlier could not maintain a low $\delta^{18}O$ value over long periods (e.g. >500 Ma). The preservation of low $\delta^{18}O$ values in the mantle source of the ELIP indicates that the mantle residence time of the subducted slab was too short for the oxygen isotopes to re-equilibrate.

In summary, our results demonstrate the influence of marine sediments in addition to an oceanic crust subducted shortly before the major melting event of the ELIP in the generation of the ELIP, causing significant chemical and isotopic heterogeneities in the rocks of the ELIP.

Based on the above geochemical and isotopic data and the tectonic framework of the western margin of the Yangtze Block, we constructed a geodynamic model of the interaction between the plume and a subducting oceanic slab that explains the geochemical and isotopic variations in the ELIP (Fig. 8). The Pan–Xi region is on the western margin of the Yangtze block (Fig. 1), near the East Paleo-Tethyan subduction zone, and recent studies show that the East Paleo-Tethyan plate was subducted eastward into the upper mantle beneath the Yangtze block until closure of the ocean during the Early Triassic (Metcalfe, 2013; Wang et al., 2018; Zhao et al., 2018). As a result, the ascending Emeishan mantle plume could have impinged on the subducting subducted Paleo-Tethyan slab at ~260 Ma (Fig. 8). The buoyancy of the large head of the mantle plume lifted the subducting Paleo-Tethyan slab, which eventually led to the broken of the up bowed slab. Variable amount of fragment of the subducted slab was incorporated into the mantle plume and returned to the base of the lithospheric mantle. During the subsequent partial melting, the geochemical and isotopic compositions of the Emeishan mantle plume were modified locally by the oceanic slab that had been altered at high temperatures and the overlying marine sediment. This interaction is recorded in the composition of some magmas in the ELIP.

5.4. *Implications for the redox heterogeneity of LIPs and the world's largest Fe–Ti–V deposit*

The Hongge intrusion, as well as other mafic–ultramafic intrusions, hosts giant Fe–Ti–V oxide deposits that comprise the largest Fe–Ti–V ore district in the world. Previous studies suggest that the early saturation of magnetite in these deposits was caused by the high fO_2 values of the parental magmas (Pang et al., 2010; Bai et al., 2012). Bai et al. (2019) reported that the oxygen fugacity of the primary magma of the ELIP is heterogeneous, with fO_2 values at the FMQ buffer to FMQ + 2.5. High-Ti picrites near the Fe–Ti–V mineralized mafic–ultramafic intrusions are among the most oxidized magmas (FMQ + 1 to FMQ + 2.5) in the ELIP, and its oxygen fugacities overlap with those of the mineralized mafic–ultramafic intrusions (Bai et al., 2019). Heterogeneous redox conditions in the primary magmas of the ELIP were further confirmed by Wu et al. (2022). These studies suggested that the variations in fO_2 were inherited from heterogeneities in the mantle source; however, the origin of redox heterogeneity in the ELIP is unclear.

Altered oceanic crust and overlying sediments contain more oxidized components (e.g. Fe^{3+}, S^{6+}, and C^{4+}) than the normal mantle (Brounce et al., 2019; Evans, 2012). Consequently, the involvement of subducted altered oceanic crust and overlying sediment in the mantle source of the ELIP could produce magma with elevated fO_2 values. We suggest that the heterogeneous redox conditions in the ELIP were maybe caused by incongruent mixing between subducted material and mantle plume material in the mantle source. The S and Fe contents of the deep ocean water and the oceanic crust were dominated by sulfide and Fe^{2+} during most of the Proterozoic, but were mostly oxidized to sulfate and Fe^{3+} after the Neoproterozoic Oxygenation Event (Shields-Zhou and Och, 2011; Stolper and Keller, 2018), which means that only plumes that incorporate subducted material younger than ~550 Ma can generate oxidized magma. The oxidized nature of the mantle source of the ELIP further indicates that a subducted slab shortly before the major melting event of the ELIP, rather than ancient recycled material, was incorporated into the mantle source of the ELIP. It is worth noting that whether the sediment contaminant in the source has an oxidizing or reducing effect much depends on the nature (e.g. organic carbon vs. carbonate) of sediment, and more work is needed to fully constrain its nature.

6. Conclusions

The marginal rocks of the Hongge intrusion have the most enriched Sr–Nd–Hf isotopic compositions of the high-Ti basaltic series in the ELIP.

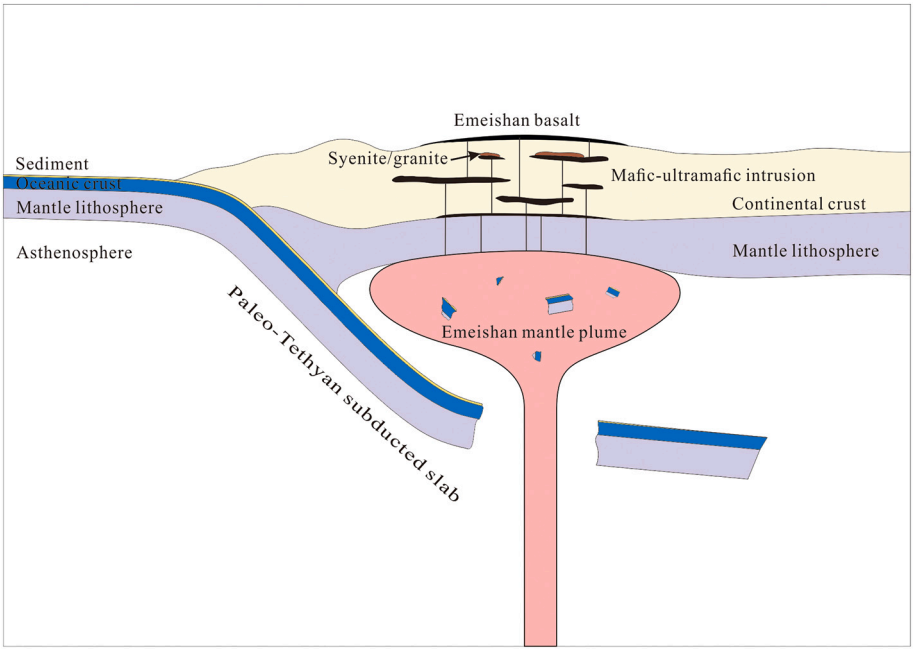

Fig. 8. Model of the interaction between the Emeishan mantle plume and the subducted Paleo-Tethyan slab.

The marginal rocks and temporally and spatially associated basalts and syenites have depleted Zr and Hf contents and there is a decoupling between their Nd and Hf isotopic compositions. These features cannot be explained by fractional crystallization or crustal contamination during magma ascent to shallow crustal levels; instead, they were inherited from the mantle source. Mixing between marine sediments and mantle peridotite in the mantle source accounts for the enriched Sr–Nd–Hf isotopic compositions, Zr—Hf depletion, and decoupling of Nd and Hf isotopic compositions in these samples as well as in other mafic–felsic intrusions of the ELIP. The low $\delta^{18}O$ values of the syenites suggest that gabbroic rocks from the lower oceanic crust that were altered at high temperatures were incorporated into the mantle source. The integrated Sr–Nd–Hf–O isotopic compositions of these mafic–felsic intrusions indicate an oceanic slab subducted shortly before the major melting event of the ELIP and overlying marine sediment were involved in the generation of the ELIP, rather than ancient recycled crustal material. Our results suggest that interaction between the mantle plume and the subducting Paleo-Tethyan slab played a substantial role in generating the geochemical and, potentially, redox heterogeneity of the ELIP.

Declaration of Competing Interest

The authors declare that they have no known competing financial interests or personal relationships that could have appeared to influence the work reported in this paper.

Data availability

Data will be made available on request.

Acknowledgments

We thank F. Xiao and YW. Chen for their help in whole-rock Sr—Nd and zircon Hf isotope analysis. This study was supported by the National Natural Science Foundation of China (42122024, 42121003 and 41873055), CAS “Light of West China” Program and Youth Innovation Promotion Association (2019391), Chinese Academy of Sciences and Innovation, K.C. Wong Education Foundation (GJTD-2020-13). Helpful and constructive reviews by the Editor Dr. Sonja Aulbach and two anonymous reviewers were greatly appreciated and significantly improved the quality of this work.

References

Aigner-Torres, M., Blundy, J., Ulmer, P., Pettke, T., 2007. Laser Ablation ICPMS study of trace element partitioning between plagioclase and basaltic melts: an experimental approach. Contrib. Mineral. Petrol. 153 (6), 647–667.
Bai, Z.-J., Zhong, H., Naldrett, A.J., Zhu, W.-G., Xu, G.-W., 2012. Whole-rock and mineral composition constraints on the genesis of the Giant hongge Fe-Ti-V oxide deposit in the emeishan Large Igneous Province, Southwest China. Econ. Geol. 107 (3), 507–524.
Bai, Z.-J., Zhong, H., Hu, R.-Z., Zhu, W.-G., Hu, W.-J., 2019. Composition of the chilled marginal rocks of the panzhihua layered intrusion, emeishan large Igneous Province, SW China: Implications for parental magma compositions, sulfide saturation history and Fe–Ti oxide mineralization. J. Petrol. 60 (3), 619–648.
Bai, Z.-J., Zhong, H., Hu, R.-Z., Zhu, W.-G., 2021. World-class Fe-Ti-V oxide deposits formed in feeder conduits by removing cotectic silicates. Econ. Geol. 116 (3), 681–691.
Bayon, G., et al., 2006. The control of weathering processes on riverine and seawater hafnium isotope ratios. Geology 34 (6), 433–436.
Bédard, J.H., 2005. Partitioning coefficients between olivine and silicate melts. Lithos 83 (3), 394–419.
Brounce, M., Cottrell, E., Kelley, K.A., 2019. The redox budget of the Mariana subduction zone. Earth Planet. Sci. Lett. 528, 115859.
Bryan, S.E., Ernst, R.E., 2008. Revised definition of large Igneous Provinces (LIPs). Earth-Sci. Rev. 86 (1–4), 175–202.
Campbell, I.H., Griffiths, R.W., 1990. Implications of mantle plume structure for the evolution of flood basalts. Earth Planet. Sci. Lett. 99 (1), 79–93.
Chauvel, C., et al., 2014. Constraints from loess on the Hf–Nd isotopic composition of the upper continental crust. Earth Planet. Sci. Lett. 388, 48–58.
Chen, J., Jahn, B.-M., 1998. Crustal evolution of southeastern China: Nd and Sr isotopic evidence. Tectonophysics 284 (1), 101–133.
Chu, Z., Chen, F., Yang, Y., Guo, J., 2009. Precise determination of Sm, Nd concentrations and Nd isotopic compositions at the nanogram level in geological samples by thermal ionization mass spectrometry. J. Anal. Atom. Spectrom 24 (11), 1534–1544.
Chung, S.-L., Jahn, B.-M., 1995. Plume-lithosphere interaction in generation of the Emeishan flood basalts at the Permian-Triassic boundary. Geology 23 (10), 889–892.
Eiler, J.M., 2001. Oxygen Isotope Variations of Basaltic Lavas and Upper Mantle Rocks. Rev. Mineral. Geochem. 43 (1), 319–364.
Eiler, J.M., et al., 1997. Oxygen isotope variations in ocean island basalt phenocrysts. Geochim. Cosmochim. Acta 61 (11), 2281–2293.
Eiler, J.M., Schiano, P., Kitchen, N., Stolper, E.M., 2000. Oxygen-isotope evidence for recycled crust in the sources of mid-ocean-ridge basalts. Nature 403 (6769), 530–534.
Ernst, R., Jowitt, S., 2013. Large igneous provinces (LIPs) and metallogeny. In: Colpron, M., Bissig, T., Rusk, B.G., Thompson, J.F.H. (Eds.), Tectonics, Metallogeny, and Discovery: The North American Cordillera and Similar Accretionary Settings: Society of Economic Geologists Special Publication, vol. 17, pp. 17–51.
Evans, K.A., 2012. The redox budget of subduction zones. Earth-Sci. Rev. 113 (1), 11–32.
Gain, S.E.M., et al., 2019. Mud tank zircon: long-term evaluation of a reference material for U-Pb Dating, Hf-isotope analysis and trace element analysis. Geostand. Geoanal. Res. 43 (3), 339–354.
Gao, S., et al., 1998. Chemical composition of the continental crust as revealed by studies in East China. Geochim. Cosmochim. Acta 62 (11), 1959–1975.
Gao, S., et al., 1999. Contrasting geochemical and Sm-Nd isotopic compositions of Archean metasediments from the Kongling high-grade terrain of the Yangtze craton: evidence for cratonic evolution and redistribution of REE during crustal anatexis. Geochim. Cosmochim. Acta 63 (13–14), 2071–2088.
Hanski, E., Kamenetsky, V.S., Luo, Z.-Y., Xu, Y.-G., Kuzmin, D.V., 2010. Primitive magmas in the Emeishan Large Igneous Province, southwestern China and northern Vietnam. Lithos 119 (1–2), 75–90.
Hart, S.R., Dunn, T., 1993. Experimental cpx/melt partitioning of 24 trace elements. Contrib. Mineral. Petrol. 113 (1), 1–8.
Hauri, E.H., Wagner, T.P., Grove, T.L., 1994. Experimental and natural partitioning of Th, U, Pb and other trace elements between garnet, clinopyroxene and basaltic melts. Chem. Geol. 117 (1–4), 149–166.
Hofmann, A.W., White, W.M., 1982. Mantle plumes from ancient oceanic crust. Earth Planet. Sci. Lett. 57 (2), 421–436.
Hou, T., Zhang, Z., Ye, X., Encarnacion, J., Reichow, M.K., 2011. Noble gas isotopic systematics of Fe–Ti–V oxide ore-related mafic–ultramafic layered intrusions in the Panxi area, China: the role of recycled oceanic crust in their petrogenesis. Geochim. Cosmochim. Acta 75 (22), 6727–6741.
Hu, Z.C., Liu, Y.S., Gao, S., Liu, W.G., Zhang, W., Xirun, T., Lin, L., Zong, K.Q., Li, M., Chen, H.H., Zhou, L., Yang, L., 2012. Improved in situ Hf isotope ratio analysis of zircon using newly designed X skimmer cone and jet sample cone in combination with the addition of nitrogen by laser ablation multiple collector ICP–MS. J. Anal. At. Spectrom. 27, 1391–1399.
Jackson, M.G., et al., 2007. The return of subducted continental crust in Samoan lavas. Nature 448 (7154), 684–687.
Jenner, G.A., 1996. Trace element geochemistry of igneous rocks: Geochemical nomenclature and analytical geochemistry. In: Wyman, D.A. (Ed.), Trace Element Geochemistry of Volcanic Rocks: Applications for Massive Sulphide Exploration. Geological Association of Canada, Short Course Notes, pp. 51–77.
Jochum, K.P., et al., 2016. Reference Values following ISO guidelines for frequently Requested Rock Reference Materials. Geostand. Geoanal. Res. 40 (3), 333–350.
Klemme, S., Günther, D., Hametner, K., Prowatke, S., Zack, T., 2006. The partitioning of trace elements between ilmenite, ulvospinel, armalcolite and silicate melts with implications for the early differentiation of the moon. Chem. Geol. 234 (3–4), 251–263.
Li, X.-H., et al., 2003. Geochemical and Nd isotopic variations in sediments of the South China Sea: a response to Cenozoic tectonism in SE Asia. Earth Planet. Sci. Lett. 211 (3), 207–220.
Li, X.H., et al., 2010. Penglai zircon megacrysts: a potential new working reference material for microbeam determination of Hf–O isotopes and U–Pb age. Geostand. Geoanal. Res. 34 (2), 117–134.
Li, X.H., et al., 2013. Qinghu zircon: a working reference for microbeam analysis of U-Pb age and Hf and O isotopes. Chin. Sci. Bull. 58, 4647–4654.
Liao, M., Tao, Y., Song, X., Li, Y., Xiong, F., 2015. Multiple magma evolution and ore-forming processes of the Hongge layered intrusion, SW China: insights from Sr-Nd isotopes, trace elements and platinum-group elements. J. Asian Earth Sci. 113 (0), 1082–1099.
Liu, J., et al., 2022. Compositional variation of picrites in the emeishan large igneous province modulated by water in the mantle plume. J. Geophys. Res. Solid Earth 127 (1), e2021JB023584.
Luan, Y., et al., 2014. Key factors controlling the accumulation of the Fe–Ti oxides in the Hongge layered intrusion in the Emeishan large Igneous Province, SW China. Ore Geol. Rev. 57 (0), 518–538.
Ma, Y., Ji, X.T., Li, J.C., Huang, M., Z, K.Z., 2003. Mineral Resources of the Panzhihua Region. Sichuan Science and Technology Press, Chengdu, p. 275.
McDonough, W., Sun, S., 1995. The composition of the Earth. Chem. Geol. 120 (3–4), 223–253.
Metcalfe, I., 2013. Gondwana dispersion and Asian accretion: Tectonic and palaeogeographic evolution of eastern Tethys. J. Asian Earth Sci. 66, 1–33.
Morel, M.L.A., Nebel, O., Nebel-Jacobsen, Y.J., Miller, J.S., Vroon, P.Z., 2008. Hafnium isotope characterization of the GJ-1 zircon reference materialby solution and laser-ablation MCICPMS. Chem. Geol. 255, 231–235.

Moussallam, Y., et al., 2019. Mantle plumes are oxidised. Earth Planet. Sci. Lett. 527, 115798.
Pang, K.-N., et al., 2010. Flood basalt-related Fe-Ti oxide deposits in the Emeishan large igneous province, SW China. Lithos 119 (1–2), 123–136.
Patchett, P.J., White, W.M., Feldmann, H., Kielinczuk, S., Hofmann, A.W., 1984. Hafnium/rare earth element fractionation in the sedimentary system and crustal recycling into the Earth's mantle. Earth Planet. Sci. Lett. 69 (2), 365–378.
Plank, T., Langmuir, C.H., 1998. The chemical composition of subducting sediment and its consequences for the crust and mantle. Chem. Geol. 145 (3), 325–394.
Qi, L., Hu, J., Gregoire, D.C., 2000. Determination of trace elements in granites by inductively coupled plasma mass spectrometry. Talanta 51 (3), 507–513.
Rehkämper, M., Hofmann, A.W., 1997. Recycled Ocean crust and sediment in Indian Ocean MORB. Earth Planet. Sci. Lett. 147 (1), 93–106.
Ren, Z.-Y., et al., 2017. Primary magmas and mantle sources of Emeishan basalts constrained from major element, trace element and Pb isotope compositions of olivine-hosted melt inclusions. Geochim. Cosmochim. Acta 208, 63–85.
Shellnutt, J.G., Wang, C.Y., Zhou, M.-F., Yang, Y.H., 2009a. Zircon Lu–Hf isotopic compositions of metaluminous and peralkaline A-type granitic plutons of the Emeishan large igneous province (SW China): Constraints on the mantle source. J. Asian Earth Sci. 35 (1), 45–55.
Shellnutt, J.G., Zhou, M.-F., Zellmer, G.F., 2009b. The role of Fe-Ti oxide crystallization in the formation of A-type granitoids with implications for the Daly gap: an example from the Permian Baima igneous complex, SW China. Chem. Geol. 259 (3–4), 204–217.
Saitoh, Y., et al., 2015. Sr, Nd, and Pb isotope compositions of hemipelagic sediment in the Shikoku Basin: Implications for sediment transport by the Kuroshio and Philippine Sea plate motion in the late Cenozoic. Earth Planet. Sci. Lett. 421, 47–57.
Shellnutt, J.G., et al., 2011. Three Fe-Ti oxide ore-bearing gabbro-granitoid complexes in the Panxi region of the Permian Emeishan large igneous province, SW China. Am. J. Sci. 311 (9), 773–812.
Shields-Zhou, G., Och, L., 2011. The case for a Neoproterozoic oxygenation event: geochemical evidence and biological consequences. GSA Today 21 (3), 4–11.
Sláma, J., et al., 2008. Plešovice zircon — A new natural reference material for U–Pb and Hf isotopic microanalysis. Chem. Geol. 249 (1), 1–35.
Song, X.-Y., et al., 2013. Formation of thick stratiform Fe-Ti oxide layers in layered intrusion and frequent replenishment of fractionated mafic magma: evidence from the Panzhihua intrusion, SW China. Geochem. Geophys. Geosyst. 14 (3), 712–732.
Spera, F.J., Bohrson, W.A., 2001. Energy-constrained open-system magmatic processes I: General model and energy-constrained assimilation and fractional crystallization (EC-AFC) formulation. J. Petrol. 42 (5), 999–1018.
Stolper, D.A., Keller, C.B., 2018. A record of deep-ocean dissolved O2 from the oxidation state of iron in submarine basalts. Nature 553 (7688), 323–327.
Sun, S.S., McDonough, W.F., 1989. Chemical and isotopic systematics of oceanic basalts: Implications for mantle composition and processes. In: Saunders, A.D., Norry, M.J. (Eds.), Magmatism in the Ocean Basins. Geological Society London Special Publications, pp. 313–345.
Tang, Q., et al., 2021. Sr-Nd-Hf-O isotope constraints on crustal contamination and mantle source variation of three Fe-Ti-V oxide ore deposits in the Emeishan large igneous province. Geochim. Cosmochim. Acta 292, 364–381.
Valley, J.W., 2003. Oxygen Isotopes in Zircon. Rev. Mineral. Geochem. 53 (1), 343–385.
Vervoort, J.D., Plank, T., Prytulak, J., 2011. The Hf–Nd isotopic composition of marine sediments. Geochim. Cosmochim. Acta 75 (20), 5903–5926.
Wang, F.L., Zhao, T., Chen, W., Wang, C., 2013. Zircon U-Pb ages and Lu-Hf isotopic compositions of the Nb-Ta-Zr bearing syenitic dikes in the Emeishan large igneous province. Acta Petrol. Sin. 29, 3519–3532.
Wang, F.L., Zhao, T., Wang, C., 2015. Petrogenisis of Permian Nb-Ta mineralized syenitic dikes in the Panxi district, SW China. Acta Petrol. Sin. 31, 1797–1805.
Wang, Y., et al., 2018. Closure of the East Paleotethyan Ocean and amalgamation of the Eastern Cimmerian and Southeast Asia continental fragments. Earth-Sci. Rev. 186, 195–230.
White, W.M., Hofmann, A.W., 1982. Sr and Nd isotope geochemistry of oceanic basalts and mantle evolution. Nature 296 (5860), 821–825.
Wu, F.-Y., Yang, Y.-H., Xie, L.-W., Yang, J.-H., Xu, P., 2006. Hf isotopic compositions of the standard zircons and baddeleyites used in U–Pb geochronology. Chem. Geol. 234 (1), 105–126.
Wu, Y.-D., et al., 2022. Redox heterogeneity of picritic lavas with respect to their mantle sources in the Emeishan large igneous province. Geochim. Cosmochim. Acta 320, 161–178.
Xu, Y.G., Chung, S.L., Jahn, B.M., Wu, G.Y., 2001. Petrologic and geochemical constraints on the petrogenesis of Permian-Triassic Emeishan flood basalts in southwestern China. Lithos 58 (3–4), 145–168.
Xiao, L., et al., 2004. Distinct mantle sources of low-Ti and high-Ti basalts from the western Emeishan large igneous province, SW China: implications for plume-lithosphere interaction. Earth Planet. Sci. Lett. 228 (3–4), 525–546.
Xu, J., et al., 2021. Low-$\delta^{18}O$ A-type granites in SW China: evidence for the interaction between the subducted Paleotethyan slab and the Emeishan mantle plume. GSA Bull. 134 (1–2), 81–93.
Yang, Y., Zhang, H., Chu, Z., Xie, L., Wu, F., 2010. Combined chemical separation of Lu, Hf, Rb, Sr, Sm and Nd from a single rock digest and precise and accurate isotope determinations of Lu–Hf, Rb–Sr and Sm–Nd isotope systems using Multi-Collector ICP-MS and TIMS. Int. J. Mass Spectrom. 290, 120–126.
Yu, S.-Y., et al., 2017. An integrated chemical and oxygen isotopic study of primitive olivine grains in picrites from the Emeishan large Igneous Province, SW China: evidence for oxygen isotope heterogeneity in mantle sources. Geochim. Cosmochim. Acta 215, 263–276.
Zhang, Z.C., et al., 2009. Petrogenetic modeling of three mafic-ultramafic layered intrusions in the Emeishan large igneous province, SW China, based on isotopic and bulk chemical constraints. Lithos 113 (3–4), 369–392.
Zhang, L., et al., 2021. Nature of the mantle plume under the emeishan large igneous province: constraints from olivine-hosted melt inclusions of the Lijiang Picrites. J. Geophys. Res. Solid Earth 126 (5), e2020JB021022.
Zhang, Z.C., Zhi, X.C., Chen, L., Saunders, A.D., Reichow, M.K., 2008. Re-Os isotopic compositions of picrites from the Emeishan flood basalt province, China. Earth Planet. Sci. Lett. 276 (1–2), 30–39.
Zhao, G., et al., 2018. Geological reconstructions of the East Asian blocks: from the breakup of Rodinia to the assembly of Pangea. Earth-Sci. Rev. 186, 262–286.
Zheng, Y.-F., Fu, B., Li, Y., Xiao, Y., Li, S., 1998. Oxygen and hydrogen isotope geochemistry of ultrahigh-pressure eclogites from the Dabie Mountains and the Sulu terrane. Earth Planet. Sci. Lett. 155 (1), 113–129.
Zhong, H., Zhu, W.-G., 2006. Geochronology of layered mafic intrusions from the Pan–Xi area in the Emeishan large igneous province, SW China. Mineral. Deposita 41 (6), 599–606.
Zhong, H., Zhu, W.-G., Chu, Z.-Y., He, D.-F., Song, X.-Y., 2007. Shrimp U-Pb zircon geochronology, geochemistry, and Nd-Sr isotopic study of contrasting granites in the Emeishan large igneous province, SW China. Chem. Geol. 236 (1–2), 112–133.
Zhong, H., et al., 2011. Timing and source constraints on the relationship between mafic and felsic intrusions in the Emeishan large igneous province. Geochim. Cosmochim. Acta 75 (5), 1374–1395.
Zhou, M.-F., Arndt, N.T., Malpas, J., Wang, C.Y., Kennedy, A.K., 2008. Two magma series and associated ore deposit types in the Permian Emeishan large igneous province, SW China. Lithos 103 (3–4), 352–368.
Zindler, A., Hart, S., 1986. Chemical geodynamics. Annu. Rev. Earth. Pl. Sc 14 (1), 493–571.
Zou, H., Li, Q.L., Bagas, L., Wang, X.C., Chen, A.Q., Li, X.H., 2021. A Neoproterozoic low-$\delta^{18}O$ magmatic ring around South China: Implications for configuration and breakup of Rodinia supercontinent. Earth Planet. Sci. Lett. 575, 117196.